

國立臺灣大學理學院應用物理研究所

碩士論文

Graduate Institute of Applied Physics

College of Science

National Taiwan University

Master Thesis



第一原理計算研究掌性外爾半金屬的自旋傳導及非線  
性光學性質

*An ab-initio study of spin transports and nonlinear optics  
of chiral Weyl semimetals XY (X=Co, Rh; Y=Si, Ge)*

謝定耘

Ting-Yun Hsieh

指導教授：郭光宇博士

Advisor: Guang-Yu Guo, Ph.D.

中華民國 111 年 9 月

September, 2022

國立臺灣大學碩士學位論文  
口試委員會審定書

第一原理計算研究掌性外爾半金屬的自旋傳導及非線  
性光學性質

An ab-initio study of spin transports and nonlinear optics  
of chiral Weyl semimetals XY (X=Co, Rh; Y=Si, Ge)

本論文係謝定耘君( R08245018 )在國立臺灣大學應用物理研究所  
完成之碩士學位論文，於民國 111 年 07 月 28 日承下列考試委員審查  
通過及口試及格，特此證明

口試委員：

郭光宇

( 簽名 )

薛克中 ( 指導教授 )

許瑋娟

詹格明

李敏正





## 誌謝

在此我想要感謝我的指導教授郭光宇老師在這三年碩士生涯的指導，讓我不只學習了固態物理的各種知識，同時也學習到做研究的方法。並且我也要謝謝實驗室的學長以及同學還有學弟們，在這幾年多虧有實驗室的大家讓我在遇到困難時有人能夠交流。最後要感謝我的家人無論是在經濟上還是精神上支持我，並在我遇到困難時鼓勵我。另外我要特別感謝實驗室的博士生 Babu Baijnath Prasad 對於這篇碩士論文自旋霍爾效應的討論以及貢獻。





## 摘要

外爾半金屬因為能帶中有被視為貝里曲率磁單極的特殊交錯而在近幾年受到注意。過渡金屬矽化物，包括一矽化鈷、一矽化鉍、一鍺化鈷和一鍺化鉍，是一組缺少鏡面對稱性質的掌性外爾半金屬。因此，這些材料的外爾結點坐落於不同的能階上。多重簡併並且擁有較大陳數的外爾結點被預言存在於這些材料中。因此，這些材料成為一個研究外爾結點跟物理性質關係的好平台。在這個論文中，我們系統性地透過第一原理計算研究以上材料的自旋霍爾效應，自旋能斯特效應還有非線性光學性質。在我們的研究中，我們展示了一鍺化鉍在所有材料中擁有最高的自旋霍爾電導率 $-139 (\hbar/e)(S/cm)$ ，並且在室溫下一矽化鈷和一鍺化鈷擁有大的自旋能斯特電導率，分別為 $-1.00 (\hbar/e)(A/mK)$ 和 $-1.25 (\hbar/e)(A/mK)$ 。非線性光學的部分，我們計算了二次階波產生還有體光伏效應。我們發現偏移電流會在低能量的區域產生峰值，而這個峰值並沒有出現在線性光學上。並且，透過我們的計算我們揭露透過調整費米能量，有可能得到被預測會發生在這個材料上的量子體光伏效應。

關鍵字: 外爾半金屬，自旋霍爾效應，自旋能斯特效應，光生伏打效應，二階非線性光學，第一原理計算。





# Abstract

Weyl semimetals have received a lot of attention in recent years because of the unique band crossing which can be seen as a monopole of Berry curvature. Among them, transition metal silicides, including CoSi, RhSi, CoGe, and RhGe, form a group of chiral Weyl semimetals with no mirror symmetry. Hence, the pairs of Weyl nodes in these materials are located at different energy levels. Also, multifold Weyl nodes with a large Chern number were predicted in these materials. Therefore, these materials should be a good platform to study the relation between these Weyl nodes and novel physical phenomena. In this thesis, we systematically study the spin Hall effect (SHE), spin Nernst effect (SNE), and nonlinear optical (NLO) effects for the above-mentioned materials by first-principles calculation. We show that the highest spin Hall conductivity (SHC) value among these materials is RhGe with  $-139 (\hbar/e)(S/cm)$ . Also, spin Nernst conductivity (SNC) at room temperature is large for both CoSi and CoGe, with the value of  $-1.00 (\hbar/e)(A/m K)$  and  $-1.25 (\hbar/e)(A/m K)$ , respectively. For NLO, second harmonic generation (SHG) and bulk photovoltaic effect (BPVE) are calculated. We find that linear shift current shows a peak in the low energy region which doesn't appear in the optical conductivity. Also, through our calculation, we reveal that by tuning Fermi energy, it is possible to get quantized circular injection current which was predicted to happen in chiral Weyl semimetals.

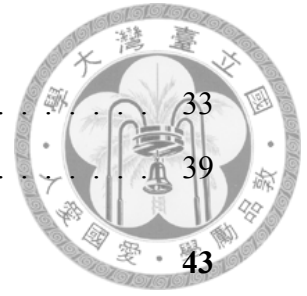
**Keywords** : Weyl semimetal, spin Hall effect, spin Nernst effect, bulk photovoltaic effect, second order nonlinear optics, first principle calculation.





# Contents

誌謝	iii
摘要	v
<b>Abstract</b>	<b>vii</b>
<b>1 Introduction</b>	<b>1</b>
1.1 Multifold chiral Weyl semimetals XY (X=Co, Rh; Y=Si, Ge) . . . . .	1
1.2 Spin Hall effect and spin Nernst effect . . . . .	4
1.3 Second order nonlinear optics . . . . .	5
<b>2 Theoretical Background</b>	<b>7</b>
2.1 Density functional theory . . . . .	7
2.2 Exchange-correlation potential . . . . .	8
2.3 Bloch theory and reciprocal lattice . . . . .	9
2.4 Berry-phase formalism for calculating intrinsic spin Hall conductivity . .	10
2.5 Formula for bulk photovoltaic effect and second harmonic generation . .	11
<b>3 Electronic structure of XY (X=Co, Rh; Y=Si, Ge)</b>	<b>13</b>
3.1 Crystal structure . . . . .	13
3.2 Computational details . . . . .	15
3.3 Electronic structure . . . . .	15
<b>4 Spin Hall effect and spin Nernst effect in XY (X=Co, Rh; Y=Si, Ge)</b>	<b>27</b>
4.1 Spin Hall effect . . . . .	27

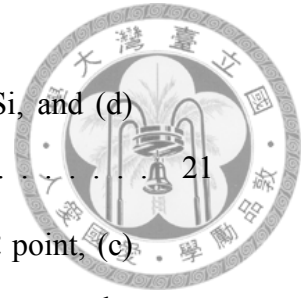


4.2 Spin Nernst effect . . . . .	33
4.3 Spin Berry curvature analysis . . . . .	39
<b>5 Nonlinear optical effects in XY (X=Co, Rh; Y=Si, Ge)</b>	<b>43</b>
5.1 Bulk photovoltaic effect . . . . .	43
5.2 Second harmonic generation . . . . .	54
<b>6 Conclusion</b>	<b>59</b>
<b>Bibliography</b>	<b>61</b>

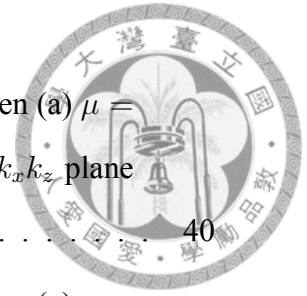


# List of Figures

1.1	Band structure of different kinds of chiral fermion nodes. (a) The traditional Weyl fermion node with $S=1/2$ , (b) spin-1 chiral fermion node, (c) spin $3/2$ RSW chiral fermion node, and (d) double Weyl fermion node. [12]	3
1.2	Schematic plot for SHE and SNE. . . . .	5
1.3	Schematic plot for SHG. . . . .	6
3.1	Simple cubic chiral crystal structure of CoSi family. (a) The primitive unit cell of CoSi family. In the primitive unit cell there are four Co/Rh and four Si/Ge atoms, respectively. (b) The view of crystal along $[111]$ axis with $2 \times 2 \times 2$ supercell. The transparency of atoms represent the depth of them. The red and blue arrows show the helicity (chirality) of atoms. Since Co/Rh atoms predominate the energy band around $E_F$ , we use the Co/Rh to define the chirality of the system. (c) First Brillouin zone of the CoSi family. . . . .	14
3.2	Total and atom-decomposed DOS for (a) CoSi, (b) CoGe, (c) RhSi, and (d) RhGe. . . . .	17
3.3	Total and atom-decomposed DOS for (a) CoSi, (b) CoGe, (c) RhSi, and (d) RhGe. . . . .	18
3.4	Band structure with SOC of (a) CoSi, (b) CoGe, (c) RhSi, and (d) RhGe. $E_F$ is at zero energy. The Chern numbers of $W_1$ , $W_2$ and $W_3$ are labeled in (a). . . . .	19
3.5	Band structure with SOC and maximally localized Wannier functions (ML-WFs) of (a) CoSi, (b) CoGe, (c) RhSi, and (d) RhGe. $E_F$ is at zero energy.	20



3.6	Band structure without SOC of (a) CoSi, (b) CoGe, (c) RhSi, and (d) RhGe. $E_F$ is at zero energy. . . . .	21
3.7	Bands structure with SOC of CoSi around (a) $\Gamma$ point, (b) $R$ point, (c) $M$ point in the Brillouin zone. The number labeled in the plot means the band Chern numbers ( $C_b$ ), which was calculated by Wanniertools [43]. The Chern number $C$ of the node is the sum over the occupied bands. . . . .	22
3.8	Bands structure with SOC of CoGe around (a) $\Gamma$ point, (b) $R$ point, (c) $M$ point in the Brillouin zone. . . . .	23
3.9	Bands structure with SOC of RhSi around (a) $\Gamma$ point, (b) $R$ point, (c) $M$ point in the Brillouin zone. . . . .	24
3.10	Bands structure with SOC of RhGe around (a) $\Gamma$ point, (b) $R$ point, (c) $M$ point in the Brillouin zone. . . . .	25
3.11	Band structure for RHC and LHC structure of CoSi. . . . .	26
4.1	Calculated SHC ( $\sigma_{xy}^z$ and $\sigma_{xz}^y$ ) for both RHC and LHC of CoSi. . . . .	28
4.2	(a, d, g)Band structure with SOC, (b, e, h) SHC ( $\sigma_{xy}^z$ and $\sigma_{xz}^y$ ) as a function of $\mu$ , and (c, f, i) SNC ( $\alpha_{xy}^z$ and $\alpha_{xz}^y$ ) as a function of $\mu$ for CoSi (a, b, c), CoGe (d, e, f) and RhSi (i, j, k), respectively. $E_F$ is at zero energy. . . . .	32
4.3	(a) Band structure with SOC, (b) SHC ( $\sigma_{xy}^z$ and $\sigma_{xz}^y$ ) as a function of $\mu$ , and (c) SNC ( $\alpha_{xy}^z$ and $\alpha_{xz}^y$ ) as a function of $\mu$ for RhGe. (d, f, h) is SBC $\Omega_{xy}^z$ and (e, g, i) is SBC $\Omega_{xz}^y$ for $\mu = E_F$ , $\mu = W_1$ , and $\mu = W_2$ , respectively. $E_F$ is at zero energy. . . . .	33
4.4	SNC of CoSi family (a) $\alpha_{xy}^z$ and (b) $\alpha_{xz}^y$ as a function of temperature $T$ when $\mu = E_F$ . . . . .	36
4.5	SNC of CoSi family (a) $\alpha_{xy}^z$ and (b) $\alpha_{xz}^y$ as a function of temperature $T$ when $\mu = W_1$ . . . . .	37
4.6	SNC of CoSi family (a) $\alpha_{xy}^z$ and (b) $\alpha_{xz}^y$ as a function of temperature $T$ when $\mu = W_2$ . . . . .	38



4.7 SBC  $\Omega_{xy}^z$  contour plot for RhGe at  $k_x k_y$  plane with  $k_z = 0$  when (a)  $\mu = E_F$ , (b)  $\mu = W_1$ , and (c)  $\mu = W_2$ . (d)  $\Omega_{xy}^z$  contour plot for  $k_x k_z$  plane with  $k_y = 0.5$  when  $\mu = W_2$ . . . . . 40

4.8 SBC  $\Omega_{xz}^y$  contour plot for RhGe at  $k_x k_y$  plane with  $k_z = 0$  when (a)  $\mu = E_F$ , (b)  $\mu = W_1$  and (c)  $\mu = W_2$ . (d)  $\Omega_{xz}^y$  contour plot for  $k_x k_z$  plane with  $k_y = 0.5$  when  $\mu = W_2$ . . . . . 41

5.1 Left hand side of the plot is the calculated linear shift current of CoSi  $\sigma_{xyz}$  with (a)  $\mu = E_F$ , (b)  $\mu = W_1$ , and (c)  $\mu = W_2$ . On the right hand side is (d) real part of optical conductivity and (e) JDOS for CoSi. . . . . 45

5.2 Left hand side of the plot is the calculated linear shift current of CoGe  $\sigma_{xyz}$  with (a)  $\mu = E_F$ , (b)  $\mu = W_1$ , and (c)  $\mu = W_2$ . On the right hand side is (d) real part of optical conductivity and (e) JDOS for CoGe. . . . . 46

5.3 Left hand side of the plot is the calculated linear shift current of RhSi  $\sigma_{xyz}$  with (a)  $\mu = E_F$ , (b)  $\mu = W_1$ , and (c)  $\mu = W_2$ . On the right hand side is (d) real part of optical conductivity and (e) JDOS for RhSi. . . . . 47

5.4 Left hand side of the plot is the calculated linear shift current of RhGe  $\sigma_{xyz}$  with (a)  $\mu = E_F$ , (b)  $\mu = W_1$ , and (c)  $\mu = W_2$ . On the right hand side is (d) real part of optical conductivity and (e) JDOS for RhGe. . . . . 48

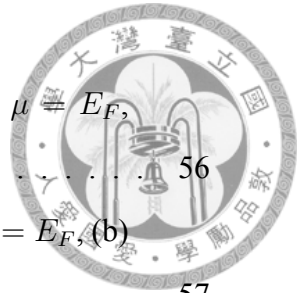
5.5 Circular injection current susceptibility  $\beta$  divide by  $\beta_0$  for CoSi when (a)  $\mu = E_F$ , (b)  $\mu = W_1$ , and (c)  $\mu = W_2$ . . . . . 50

5.6 Circular injection current susceptibility  $\beta$  divide by  $\beta_0$  for CoGe when (a)  $\mu = E_F$ , (b)  $\mu = W_1$ , and (c)  $\mu = W_2$ . . . . . 51

5.7 Circular injection current susceptibility  $\beta$  divide by  $\beta_0$  for RhSi when (a)  $\mu = E_F$ , (b)  $\mu = W_1$ , and (c)  $\mu = W_2$ . . . . . 52

5.8 Circular injection current susceptibility  $\beta$  divide by  $\beta_0$  for RhGe when (a)  $\mu = E_F$ , (b)  $\mu = W_1$ , and (c)  $\mu = W_2$ . . . . . 53

5.9 Real, imaginary, and absolute value of SHG of CoSi with (a)  $\mu = E_F$ , (b)  $\mu = W_1$ , and (c)  $\mu = W_2$ . . . . . 55



5.10 Real, imaginary, and absolute value of SHG of CoGe with (a)  $\mu = E_F$ ,  
(b)  $\mu = W_1$ , and (c)  $\mu = W_2$ . . . . . 56

5.11 Real, imaginary, and absolute value of SHG of RhSi with (a)  $\mu = E_F$ , (b)  
 $\mu = W_1$ , and (c)  $\mu = W_2$ . . . . . 57

5.12 Real, imaginary, and absolute value of SHG of RhGe with (a)  $\mu = E_F$ ,  
(b)  $\mu = W_1$ , and (c)  $\mu = W_2$ . . . . . 58



# List of Tables

3.1	Atom positions of RHC [33] and LHC [34] of CoSi. The lattice constant of both RHC and LHC is $4.45\text{\AA}$ . . . . .	14
3.2	Experiment lattice constants of the CoSi family that we use in our calculations in this thesis. . . . .	14
4.1	Tensor shape of SHC for $P2_13$ space group with RHC and LHC, there are only two independent nonzero tensor elements $\sigma_{xy}^z$ and $\sigma_{xz}^y$ . Note that SNC has the same independent elements as SHC. . . . .	29
4.2	Calculated SHC and SNC at $T = 300K$ for all four CoSi family materials. SHC and SNC from previously studied Weyl semimetal TaAs, Dirac semimetal ZrSiS, and transition metal Pt are also in the list. We also show the experimental measurement of electrical conductivity $\sigma_{xx}^c$ and Seebeck coefficient $S_{xx}$ used for calculating spin Hall angle $\Theta_{sH}$ and spin Nernst angle $\Theta_{sN}$ . . . . .	29
4.3	Energy levels of Weyl fermion nodes $W_1$ , $W_2$ , and $W_3$ for each materials. SHC ( $\sigma_{xy}^z$ and $\sigma_{xz}^y$ ) and SNC ( $\alpha_{xy}^z$ and $\alpha_{xz}^y$ ) at $T = 300K$ after shifting $\mu$ to $W_1$ and $W_2$ are also listed in the table. Note that the values in the parentheses mean $\mu = W_2$ . . . . .	30





# Chapter 1

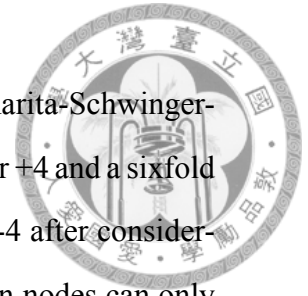
## Introduction

### 1.1 Multifold chiral Weyl semimetals XY (X=Co, Rh; Y=Si, Ge)

In the past few years, topological materials, including Dirac semimetals (DSMs) and Weyl semimetals (WSMs), have attracted a lot of attention due to their unique electronic structure. To be more specific, linear band crossing appear in these materials which are called Weyl nodes or Dirac nodes. For DSMs, the band structure hosts a linear crossing point which can be described by  $4 \times 4$  Dirac Hamiltonian [1]. On the other hand, for WSMs, because either time-reversal symmetry or inversion symmetry is broken the Dirac node splits and two Weyl nodes appear in the band structure simultaneously, which can be described by  $2 \times 2$  Weyl Hamiltonian[1]. This pair of Weyl nodes is seen as source (positive Chern number) or sink (negative Chern number) of Berry curvature in the materials. As a result, tons of studies were carried out to investigate the physics behind the materials [2, 3, 4, 5, 6, 7, 8, 9, 53, 11].

Recently, CoSi [12] and RhSi [13] were predicted to host unconventional Weyl nodes in their band structure. Instead of a double degenerate linear crossing with Chern number  $\pm 1$ , semimetals XY (X=Co, Rh; Y=Si, Ge) have a threefold degenerate spin-1 chiral fermion node [see Fig. 1.1(b)] with Chern number +2 at  $\Gamma$  and a fourfold degenerate double Weyl node [see Fig. 1.1(d)] at  $R$  with Chern number -2 without spin-orbit coupling

(SOC). The nodes will further split into a fourfold degenerate spin-3/2 Rarita-Schwinger-Weyl (RSW) chiral fermion node at  $\Gamma$  [see Fig. 1.1(c)] with Chern number +4 and a sixfold degenerate double spin-1 chiral fermion node at  $R$  with Chern number -4 after considering SOC. Unlike traditional Weyl nodes, the spin-1 and spin-3/2 fermion nodes can only be realized under the symmetry restriction of crystal and are not allowed in high energy physics [12]. Also, since the materials lack mirror symmetry, the Weyl nodes are located at different energy levels which can lead to some interesting phenomena such as quantized circular photogalvanic effect (CPGE) [6, 8, 14, 15]. Fig. 1.1 shows the band structure for different types of Weyl nodes.



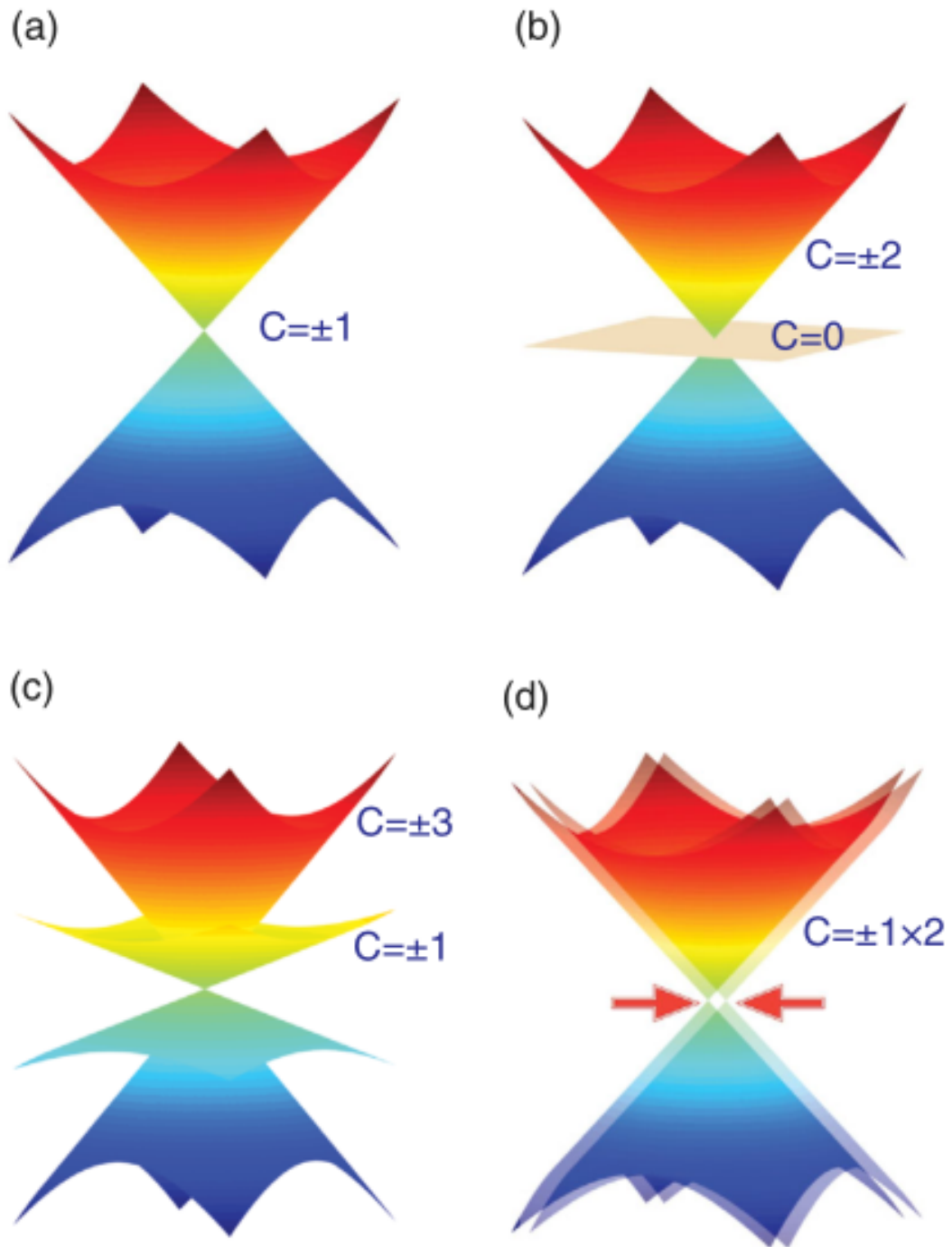


Figure 1.1: Band structure of different kinds of chiral fermion nodes. (a) The traditional Weyl fermion node with  $S=1/2$ , (b) spin-1 chiral fermion node, (c) spin 3/2 RSW chiral fermion node, and (d) double Weyl fermion node. [12]



## 1.2 Spin Hall effect and spin Nernst effect

The ordinary Hall effect [see Fig. 1.2(a)] is a well-known phenomenon that, when current goes through a material under a perpendicular magnetic field, electrons accumulate at one side due to Lorentz force and hence induce Hall voltage. On the other hand, the spin Hall effect (SHE) was proposed by Dyakonov and Perel in 1971 [16]. In a non-magnetic material even without any external magnetic field, spin-up and spin-down electrons still move to the different sides because of SOC, and thus form pure spin current [see Fig. 1.2(c)]. Because Weyl nodes are the source or sink of Berry curvature in the material and spin Hall conductivity (SHC) is the interplay between spin operator and Berry curvature, we can expect that WSMs may host large SHC. For example, WSMs TaAs was predicted to have large SHC by first principle calculations [2], and large SHC was also observed in WSMs WTe<sub>2</sub> [57, 58, 11].

Besides driving the electrons with the electric field, the other choice is applying a temperature gradient to the material. Similarly, the above mention features will also show up in this case, which would be called the Nernst effect [see Fig. 1.2(d)] and spin Nernst effect (SNE) [see Fig. 1.2(f)] [17], respectively. In fact, since the origin of SHE and SNE is all coming from SOC, we can expect that material with large SHE would also present large SNE. The detailed formalism of evaluating the value of SHE and SNE will be introduced explicitly in chapter 2.

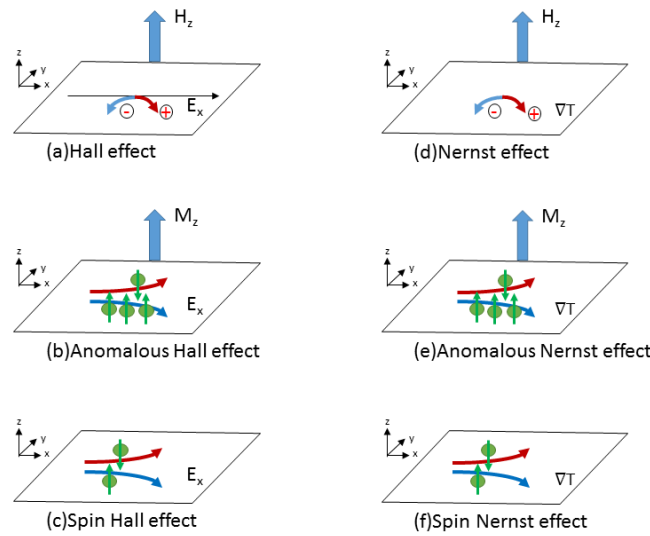


Figure 1.2: Schematic plot for SHE and SNE.

### 1.3 Second order nonlinear optics

Optical effects are another topic that has been studied a lot for a long period. The optical response relation between material's polarization  $P$  and electric field  $E$  can be written down as[18]

$$P = \epsilon_0[\chi^{(1)}E_a + \chi^{(2)}E_aE_b + \chi^{(3)}E_aE_bE_c + \dots], \quad (1.1)$$

where  $\chi$  represents the susceptibility. In the first term of the formula  $\chi^{(1)}$  is the traditional linear susceptibility, and the following terms are nonlinear susceptibilities. In a system under inversion symmetry, the even-order terms of optical effects vanish due to  $P(\vec{r}) = -P(-\vec{r})$  and  $E(\vec{r}) = -E(-\vec{r})$ , which implies that susceptibilities of even terms should be zero. As a result, to produce second order nonlinear effects, it's necessary to find a material with inversion symmetry breaking.

In this thesis, we will focus on two kinds of second order nonlinear optical effect, which is the second harmonic generation (SHG) and bulk photovoltaic effect (BPVE). For SHG [18], it is an effect that when two photons with energy  $\hbar\omega$  hit the materials, they will be absorbed and then the materials will emit photons with double frequency  $2\hbar\omega$  [see Fig. 1.3]. And BPVE is a nonlinear optical effect that generates photocurrent after

absorbing the light. We will have a deeper discussion of the formula and mechanism of these effects in chapter 2.

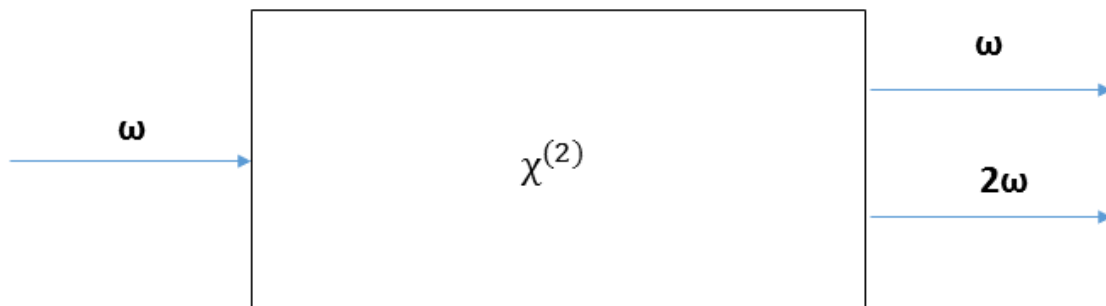


Figure 1.3: Schematic plot for SHG.



## Chapter 2

# Theoretical Background

### 2.1 Density functional theory

In quantum mechanics, it's simple to solve a single particle Schödinger equation and get the wavefunction to predict the behavior of the system. However, in condensed matter physics, things become more tricky because it's difficult to explicitly solve Schödinger equation if not impossible for a many-body system. As a result, density functional theory (DFT) is a method that can help us simplify the equation and get an approximation answer. Here we start from the normal Schödinger equation of a many-body system.

$$\begin{aligned} H\Psi = & \left[ \sum_{i=1}^N \left( -\frac{\hbar^2}{2m_e} \vec{\nabla}_{i^2} \right) + \sum_{I=1}^M \left( -\frac{\hbar^2}{2m_I} \vec{\nabla}_{i^2} \right) - \sum_{i=1}^N \sum_{I=1}^M \left( \frac{Z_I e^2}{|\vec{r}_i - \vec{R}_I|} \right) + \sum_{i,j=1, i < j}^N \left( \frac{e^2}{|\vec{r}_i - \vec{r}_j|} \right) \right. \\ & \left. + \sum_{I,J=1, I < J}^M \left( \frac{Z_I Z_J e^2}{|\vec{R}_I - \vec{R}_J|} \right) \right] \Psi. \end{aligned} \tag{2.1}$$

The first two terms in the formula are kinetic energy of electrons and nuclei, and the last three terms are interaction terms between electrons and nuclei, between electrons and electrons, and also between nuclei and nuclei. Here we use Born-Oppenheimer approximation, which assumes that nuclei are heavy and their positions are fixed. The kinetic term of nuclei should become zero and the nuclei-nuclei interaction term become a constant. Thus



we can simplify the formula as

$$H\psi = \left[ \sum_{i=1}^N \left( -\frac{\hbar^2}{2m_e} \nabla_i^2 \right) + \sum_{i=1}^N V_{ext}(\vec{r}_i) + \sum_{i,j=1, i<j}^N U(\vec{r}_i, \vec{r}_j) \right] \Psi = [T + V + U] \Psi. \quad (2.2)$$

Only terms that involve electrons are left,  $T$  is the kinetic energy term,  $V$  is the electron-nuclei interaction term, and  $U$  is the electron-electron interaction energy term. The difficult part of solving this equation is the electron-electron interaction term which can be really complicated in real systems. To simplify it, we further define electron density distribution as [19]

$$n(\vec{r}_1) = \int d\vec{r}_2^3 \int d\vec{r}_3^3 \cdots \int d\vec{r}_N^3 |\psi(\vec{r}_1, \vec{r}_2 \cdots \vec{r}_N)|^2. \quad (2.3)$$

In 1964 Hohenberg and Kohn established two theorems that are important for DFT [19]. The first one is that the ground state energy of a system should be a unique functional of electron density  $n(\vec{r})$ , and the second one is that the electron density that minimizes the energy of the system should be the real electron density of it. With this information now we can simplify the equation as

$$[T + V + \int \frac{n(\vec{r}')}{|\vec{r} - \vec{r}'|} d\vec{r}'^3 + V_{xc}(\vec{r})] \psi_i(\vec{r}) = \epsilon_i \psi_i(\vec{r}). \quad (2.4)$$

This is called Kohn-Sham equation [20],  $V_{xc}$  is the exchange-correlation potential which is the only unknown part of the equation.

## 2.2 Exchange-correlation potential

After simplifying the formula [Eq. (2.4)], the last thing that we need to solve is finding exchange-correlation potential. To date, there are several successful approximations to deal with the problem. Two of them are local density approximation (LDA) [21] and generalized gradient approximations (GGA) [22]. For LDA method, the exchange-correlation



energy is

$$E_{xc}[n] = \int \epsilon_{xc}[n]n(\vec{r})d^3\vec{r}, \quad (2.5)$$

where

$$\epsilon_{xc}[n] = \epsilon_{xc}(n(\vec{r})) \quad (2.6)$$

is exchange-correlation energy per particle of homogeneous electron gas with density  $(n(\vec{r}))$ . And the exchange-correlation potential  $V_{xc}$  can be calculated by using relation

$$V_{xc} = \frac{\partial E_{xc}[n]}{\partial n}. \quad (2.7)$$

However, LDA is kind of a simple approximation to solve the problem. As a result, GGA method improves the accuracy by expanding the electron density to gradient term.

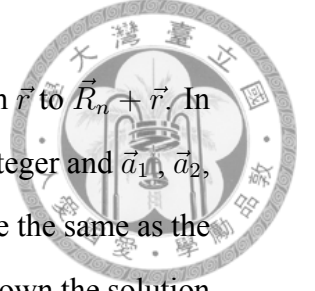
$$\epsilon_{xc}[n] = \epsilon_{xc}(n(\vec{r}), \vec{\nabla}n(\vec{r})). \quad (2.8)$$

One famous example showcasing the difference between these two methods is the calculation of Iron [23, 24, 25]. LDA predicts that Iron has non-magnetic ground state and has FCC structure, which is wrong. However, GGA successfully gets magnetic ground state and BCC structure, which is correct. Nowadays, there are several versions of GGA provided to the users. In this thesis, we use Perdew-Burke-Ernzerhof (PBE) [22] version to do the calculations.

## 2.3 Bloch theory and reciprocal lattice

Bloch theory [26] is one of the key concepts in solid-state physics. Because of the periodic nature of crystal, we can easily claim that the wavefunction of Schödinger equation should also obey this feature, which we call translation symmetry. Let's start with a normal translation operator

$$\hat{T}(\vec{R}_n)|\vec{r}\rangle = |\vec{R}_n + \vec{r}\rangle. \quad (2.9)$$



The above formula means that the operator makes the position shift from  $\vec{r}$  to  $\vec{R}_n + \vec{r}$ . In the crystal, if  $\vec{R}_n$  is equal to  $n_1\vec{a}_1 + n_2\vec{a}_2 + n_3\vec{a}_3$ , where  $n_1, n_2, n_3$  are integer and  $\vec{a}_1, \vec{a}_2, \vec{a}_3$  are primitive lattice vectors, respectively. The wavefunction should be the same as the original due to periodic nature we mention before. Hence we can write down the solution to Schödinger equation in crystal as

$$\psi(\vec{r}) = e^{i\vec{k}\cdot\vec{r}}u(\vec{r}), \quad (2.10)$$

where  $u(\vec{r})$  is a periodic function that  $u(\vec{r}) = u(\vec{r} + n \cdot \vec{a})$ , and  $e^{i\vec{k}\cdot\vec{r}}$  is a plane wave. Also notice that  $\vec{k}$  is crystal momentum where  $\vec{k} = x_1\vec{b}_1 + x_2\vec{b}_2 + x_3\vec{b}_3$  and  $x_1, x_2, x_3 < 0$ . Here  $\vec{b}_1, \vec{b}_2$  and  $\vec{b}_3$  are called primitive reciprocal lattice vectors, and they are related to the primitive lattice vectors as

$$\vec{a}_i \cdot \vec{b}_j = 2\pi\delta_{ij}. \quad (2.11)$$

With primitive reciprocal lattice vectors, we can thus define the first Brillion zone. By plotting eigenvalue energy in the first Brillion zone, we can get the band structure of the material.

## 2.4 Berry-phase formalism for calculating intrinsic spin Hall conductivity

For the intrinsic SHC, it can be calculated quite straightforwardly by using Berry-phase formalism [27, 28]. First, SHC is a third-rank tensor that

$$\sigma_{ij}^s = J_i^s / E_j, \quad (2.12)$$

where  $i, j \in (x, y, z)$  but  $i \neq j$ . In this equation, the upper index  $s$  denotes the spin direction,  $J_i^s$  is the  $i^{th}$  component of spin current density with spin polarize along  $s$  direction and  $E_j$  is the  $j^{th}$  component of an electric field. With the Berry-phase formalism, we can



calculate SHC by integrating spin Berry curvature of all occupied bands [27].

$$\sigma_{ij}^s = e \sum_n \int_{BZ} \frac{dk}{(2\pi)^3} f_{\mathbf{k}n} \Omega_{ij}^{n,s}(k), \quad (2.13)$$

$$\Omega_{ij}^{n,s}(\mathbf{k}) = \sum_{n' \neq n} \frac{2Im[\langle \mathbf{k}n | \{\tau_s, v_i\} / 4 | \mathbf{k}n' \rangle \langle \mathbf{k}n' | v_j | \mathbf{k}n \rangle]}{(\epsilon_{\mathbf{k}n} - \epsilon_{\mathbf{k}n'})^2 + (\eta)^2}, \quad (2.14)$$

where  $f_{\mathbf{k}n}$  is Fermi-Dirac distribution,  $\Omega_{ij}^{n,s}(\mathbf{k})$  is spin Berry curvature for the  $n^{\text{th}}$  band,  $\tau_s$  is Pauli matrix,  $v_i$  is velocity operator and  $\eta$  is fixed smearing parameter. Similar to SHC tensor, SNC tensor is also a thrid-rank tensor that

$$\alpha_{ij}^s = -J_i^s / \nabla_j T. \quad (2.15)$$

Just replacing electric field  $E_j$  with temperature gradient  $\nabla_j T$ . In this thesis, we calculate SNC directly through energy integration of SHC [29]

$$\alpha_{ij}^s = \frac{1}{e} \int_{-\infty}^{\infty} d\varepsilon \frac{\partial f}{\partial \varepsilon} \sigma_{ij}^s(\varepsilon) \frac{\varepsilon - \mu}{T}. \quad (2.16)$$

## 2.5 Formula for bulk photovoltaic effect and second harmonic generation

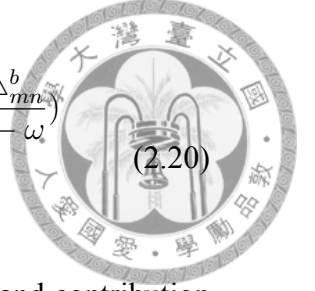
For the NLO properties, we use the length-gauge formulism derived by Aversa and Sipe [30]. In the thesis, we will mainly focus on SHG and BPVE. SHG can be written down as

$$P_a^{(2)}(\omega) = \chi_{(abc)}^{(2)}(-2\omega; \omega, \omega) \varepsilon_b(\omega) \varepsilon_c(\omega), \quad (2.17)$$

where  $\chi_{(abc)}^{(2)}(-2\omega; \omega, \omega)$  is SHG susceptibility, and it can be further divided into two parts

$$\chi_{(abc)}^{(2)}(-2\omega; \omega, \omega) = \chi_{(abc),e}^{(2)}(-2\omega; \omega, \omega) + \chi_{(abc),i}^{(2)}(-2\omega; \omega, \omega), \quad (2.18)$$

$$\chi_{(abc),e}^{(2)}(-2\omega; \omega, \omega) = \frac{e^3}{\varepsilon \hbar^2 V_c} \sum_{n,m,l} \sum_k \frac{r_{mn}^a}{\omega_{mn} - 2\omega} \left( \frac{r_{ml}^b r_{ln}^a f_{nl}}{\omega_{ln} - \omega} - \frac{r_{ml}^c r_{ln}^b f_{lm}}{\omega_{ml} - \omega} \right), \quad (2.19)$$



$$\begin{aligned} \chi_{(abc),i}^{(2)}(-2\omega; \omega, \omega) = & \frac{ie^3}{\varepsilon \hbar^2 V_c} \sum_{n,m} \sum_k \left[ \frac{f_{nm} r_{nm}^a}{\omega_{mn} - 2\omega} \left( \frac{r_{mn;b}^c}{\omega_{mn} - \omega} - \frac{r_{mn}^c \Delta_{mn}^b}{\omega_{mn} - \omega} \right) \right. \\ & \left. - \frac{f_{nm} r_{mn}^c}{2(\omega_{mn} - \omega)} \left( \frac{r_{nm;a}^b}{\omega_{mn} + \omega} - \frac{r_{nm} \Delta_{mn}^a}{(\omega_{ml} - \omega)^2} \right) \right], \end{aligned} \quad (2.20)$$

where  $\chi_{(abc),i}$  and  $\chi_{(abc),e}$  is pure interband contribution and inter-intraband contribution for SHG susceptibility, respectively. Subscribe  $n, m, l$  denote the  $n^{th}$ ,  $m^{th}$ , and  $l^{th}$  band. The BPVE [31, 32] is an effect that materials generate photocurrent after absorbing light. In the clean limit, we can write down

$$j_{dc}^c = \sigma_{dc}^{c;ab}(\omega) E_a(\omega) E_b(-\omega), \quad (2.21)$$

$$\sigma_{dc}^{c;ab}(\omega) = \sigma_{shift}^{c;ab}(\omega) + \sigma_{inj}^{c;ab}(\omega). \quad (2.22)$$

There are two categories of BPVE [32], one is shift current and the other is injection current. The mechanism of shift current is the shift of electron while doing interband transition, and injection current can be seen as velocity difference for excited electrons. Both of them have a real part and an imaginary part. The real part which is triggered by linearly polarized light is called linear shift current or linear injection current, and the imaginary part due to circularly polarized light is called circular shift current or circular injection current. These quantities can be calculated with formula [32]

$$\sigma_{shift}^{c;ab}(\omega) = -\frac{\pi e^3}{\hbar^2} \int_k \sum_{n,m} f_{nm}^{FD} (R_{mn}^{c,a} - R_{nm}^{c,b}) r_{nm}^b r_{mn}^a \delta(\omega_{mn} - \omega), \quad (2.23)$$

$$\sigma_{inj}^{c;ab}(\omega) = -\tau \frac{2\pi e^3}{\hbar^2} \int_k \sum_{n,m} f_{nm}^{FD} \Delta_{mn}^c r_{nm}^b r_{mn}^a \delta(\omega_{mn} - \omega), \quad (2.24)$$

where  $f_{nm}^{FD}$  is Fermi-Dirac distribution.  $R_{mn}^{c,a}$  is called shift vector which is the crucial part of shift current, its definition is  $R_{mn}^{c,a} = r_{mm}^c - r_{nn}^c + i\partial_c \text{Log}(r_{mn}^a)$ , and  $\Delta_{mn}^c = v_{mm}^c - v_{nn}^c$ .



## Chapter 3

# Electronic structure of XY (X=Co, Rh; Y=Si, Ge)

### 3.1 Crystal structure

The structure of the CoSi family is a simple cubic crystal with  $P2_13$  space group [33, 34]. Interestingly, they are structurally chiral. There are two kinds of handedness, right-handed crystal (RHC) or left-handed crystal (LHC) [34], based on the view along the [111] axis shown in Fig. 3.1. However, whether it is RHC or LHC is decided by the nature of the crystal and the growing method. Based on the experiment, we only find that CoSi has successfully grown in both RHC [33] and LHC [34]. For the other materials, they are all RHC [35, 36, 37]. This makes CoSi a good platform to study how the structural chirality affects the physical properties. The experimental lattice constants are used in the present calculations and are listed in Table 3.1 and Table 3.2.

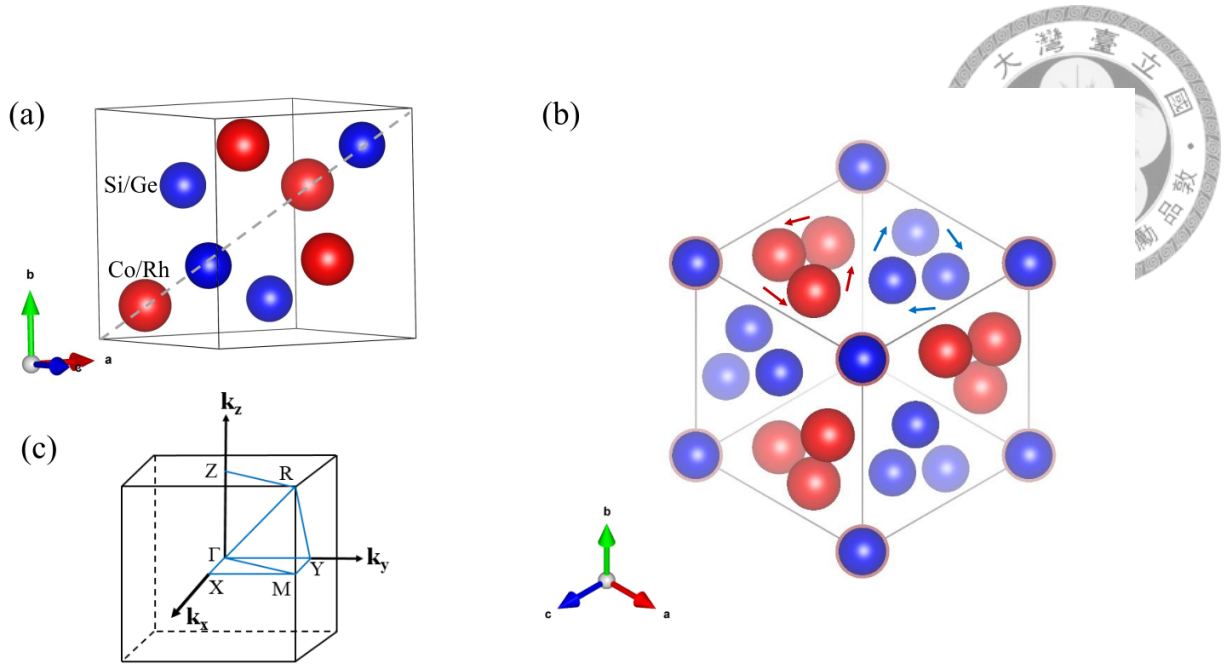


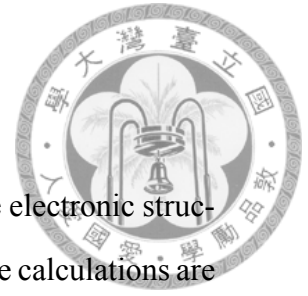
Figure 3.1: Simple cubic chiral crystal structure of CoSi family. (a) The primitive unit cell of CoSi family. In the primitive unit cell there are four Co/Rh and four Si/Ge atoms, respectively. (b) The view of crystal along  $[111]$  axis with  $2 \times 2 \times 2$  supercell. The transparency of atoms represent the depth of them. The red and blue arrows show the helicity (chirality) of atoms. Since Co/Rh atoms predominate the energy band around  $E_F$ , we use the Co/Rh to define the chirality of the system. (c) First Brillouin zone of the CoSi family.

atom	Left-handed crystal (LHC)			Right-handed crystal (RHC)		
	x	y	z	x	y	z
Co	0.3934	0.3934	0.3934	0.1400	0.1400	0.1400
Co	0.1066	0.6066	0.8934	0.3600	0.8600	0.6400
Co	0.6066	0.8934	0.1066	0.8600	0.6400	0.3600
Co	0.8934	0.1066	0.6066	0.6400	0.3600	0.8600
Si	0.0935	0.0935	0.0935	0.8430	0.8430	0.8430
Si	0.4065	0.9065	0.5935	0.6570	0.1570	0.3430
Si	0.9065	0.5935	0.4065	0.1570	0.3430	0.6570
Si	0.5935	0.4065	0.9065	0.3430	0.6570	0.1570

Table 3.1: Atom positions of RHC [33] and LHC [34] of CoSi. The lattice constant of both RHC and LHC is  $4.45\text{\AA}$ .

Structure	a( $\text{\AA}$ )
CoSi [33]	4.450
CoGe [35]	4.631
RhSi [36]	4.674
RhGe [37]	4.862

Table 3.2: Experiment lattice constants of the CoSi family that we use in our calculations in this thesis.



## 3.2 Computational details

In this thesis, we use Vienna *ab initio* package (VASP) [38, 39] to do the electronic structure calculations, including band structure and density of state (DOS). The calculations are based on the density functional theory with the generalized gradient approximation (GGA) [22]. A large energy cutoff 400 eV was used in these calculations. The valence electronic configurations of the pseudopotentials for Co, Rh, Si, and Ge are  $3d^84s^1$ ,  $4d^85s^1$ ,  $3s^23p^2$ , and  $3d^{10}4s^24p^2$ , respectively. In the self-consistent band structure calculation we use  $\Gamma$ -centered k-mesh of  $16 \times 16 \times 16$  in the Brillouin zone, and k-mesh of  $24 \times 24 \times 24$  for DOS to get a more accurate result. After that, Wannier90 package [40, 41, 42] is used to construct tight-binding Hamiltonian with  $d_{xy}$  orbitals of transition metal from -0.5 eV below Fermi level ( $E_f$ ) to 0.5 eV above  $E_f$  and is further used to calculate SHC and NLO. For SHC, k-mesh of  $200 \times 200 \times 200$  with  $5 \times 5 \times 5$  refinement is used with adaptive smearing. For NLO, k-mesh of  $200 \times 200 \times 200$  is used.

## 3.3 Electronic structure

All XY crystals in this thesis have a non-magnetic ground state. Calculated DOS and band structure for both with and without SOC are plotted in Figs. 3.2-3.10 below. From DOS [see Figs. 3.2 and 3.3] we can see that all four materials have a pretty low value of DOS around  $E_f$ , which indicate that they are all semimetals. Also around the  $E_f$ , the  $d$  orbitals of Co or Rh dominate the contribution. Due to the symmetry of the crystal, multifold degenerate nodes are guaranteed at  $\Gamma$  point and  $R$  point. When we don't consider SOC [see Fig. 3.6], three-fold degenerate spin-1 fermion node with Chern number +2 appears at  $\Gamma$ , and four-fold degenerate double Weyl fermion node with Chern number -2 appears at  $R$ . However, when SOC is added [see Fig. 3.4], these bands split into higher degeneracies with a higher Chern number. To be specific, the spin-1 fermion node at  $\Gamma$  will split into a four-fold degenerate spin-3/2 RSW fermion node ( $W_1$ ) with Chern number +4 and a normal Weyl node ( $W_3$ ) with Chern number +1. The four-fold degenerate double Weyl fermion node at  $R$  split into a six-fold degenerate spin-1 double Weyl fermion



node ( $W_2$ ) with Chern number -4. Notice that spin-3/2 RSW fermion and spin-1 fermion have no counterpart in high-energy physics, and thus they are called unconventional chiral fermions. These unconventional chiral fermions, especially the one at  $\Gamma$ , are located near  $E_f$ , which make it a good platform to study novel physics effects related to chiral fermions with doping electrons or holes.

Another interesting thing is that we also calculate band structure for LHC CoSi, and we find that the band structure is almost the same as the RHC [see Fig. 3.11]. Nevertheless, the signs of the Chern numbers of these Weyl nodes are all reversed, which means that for RHC Chern numbers of  $W_1$ ,  $W_2$ , and  $W_3$  are -4, +4, and -1, respectively.

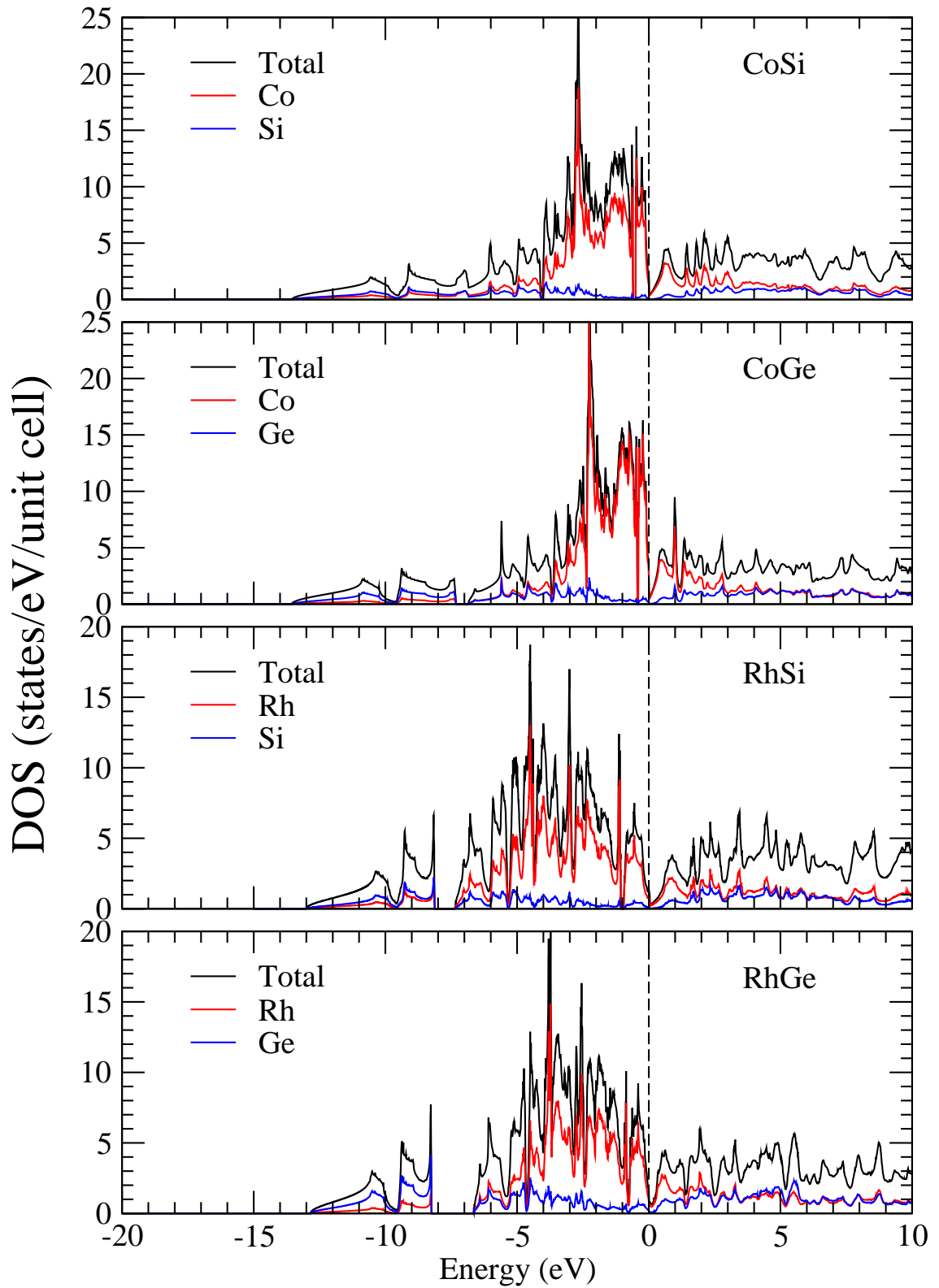


Figure 3.2: Total and atom-decomposed DOS for (a) CoSi, (b) CoGe, (c) RhSi, and (d) RhGe.

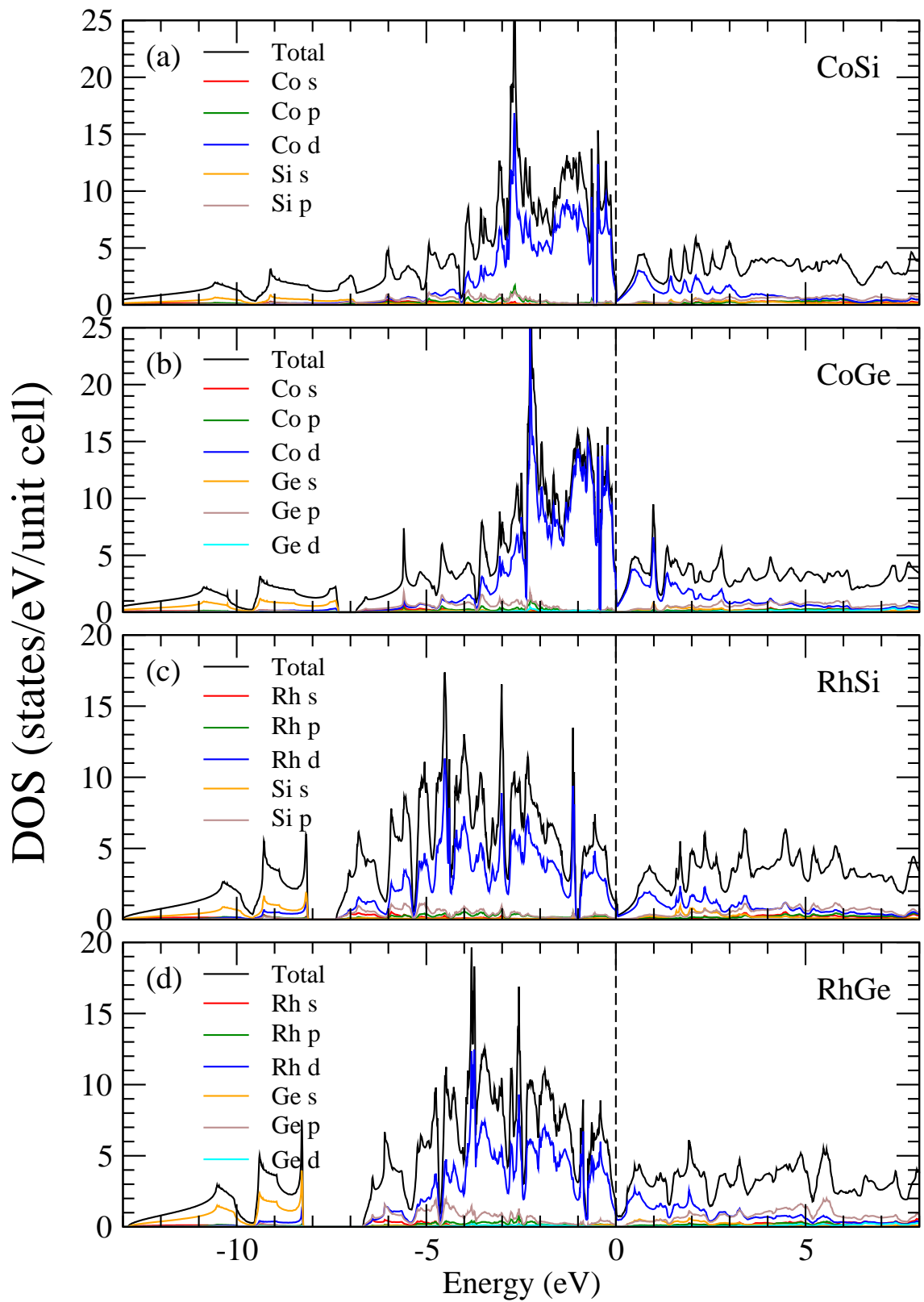


Figure 3.3: Total and atom-decomposed DOS for (a) CoSi, (b) CoGe, (c) RhSi, and (d) RhGe.

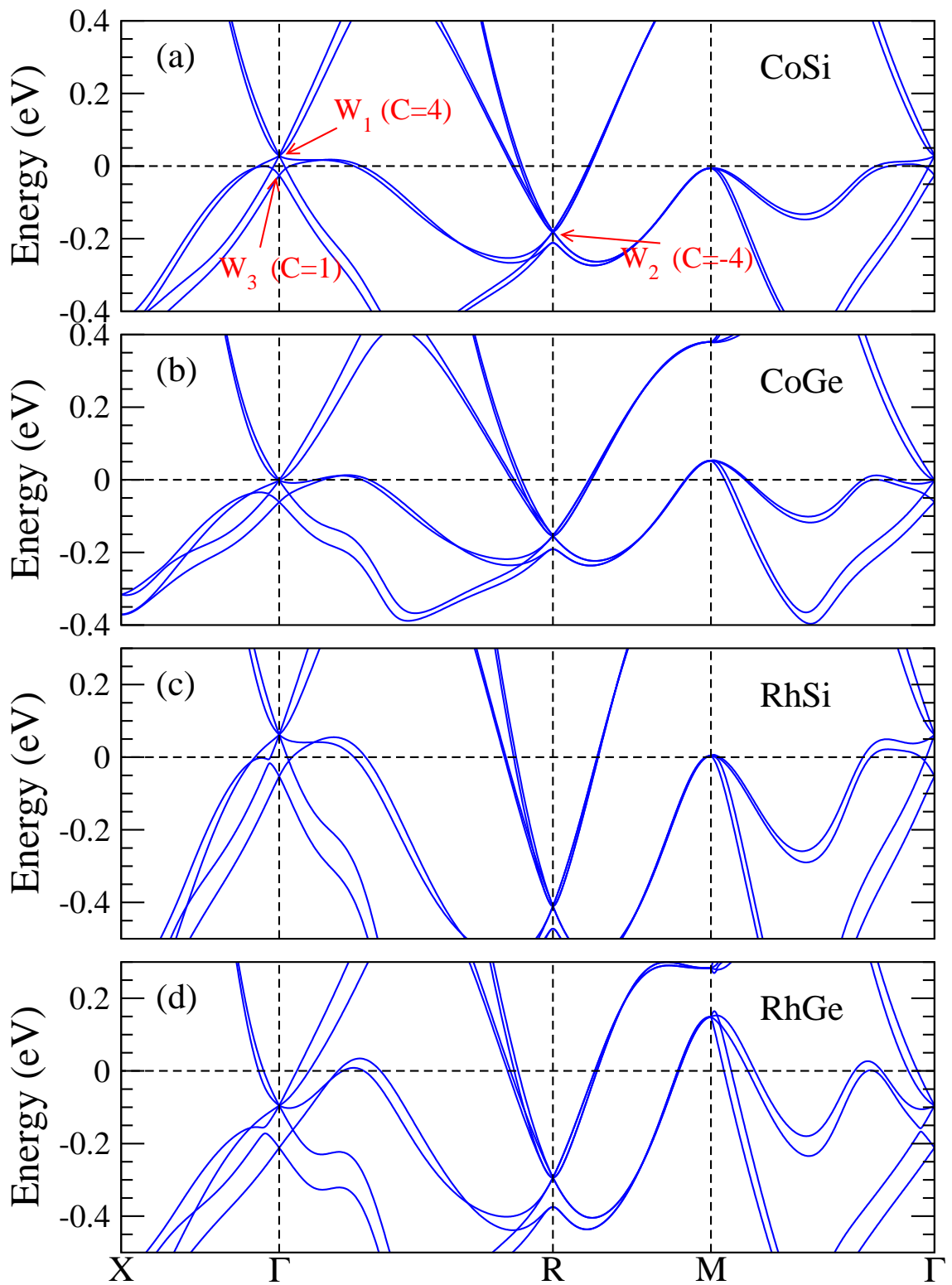


Figure 3.4: Band structure with SOC of (a) CoSi, (b) CoGe, (c) RhSi, and (d) RhGe.  $E_F$  is at zero energy. The Chern numbers of  $W_1$ ,  $W_2$  and  $W_3$  are labeled in (a).

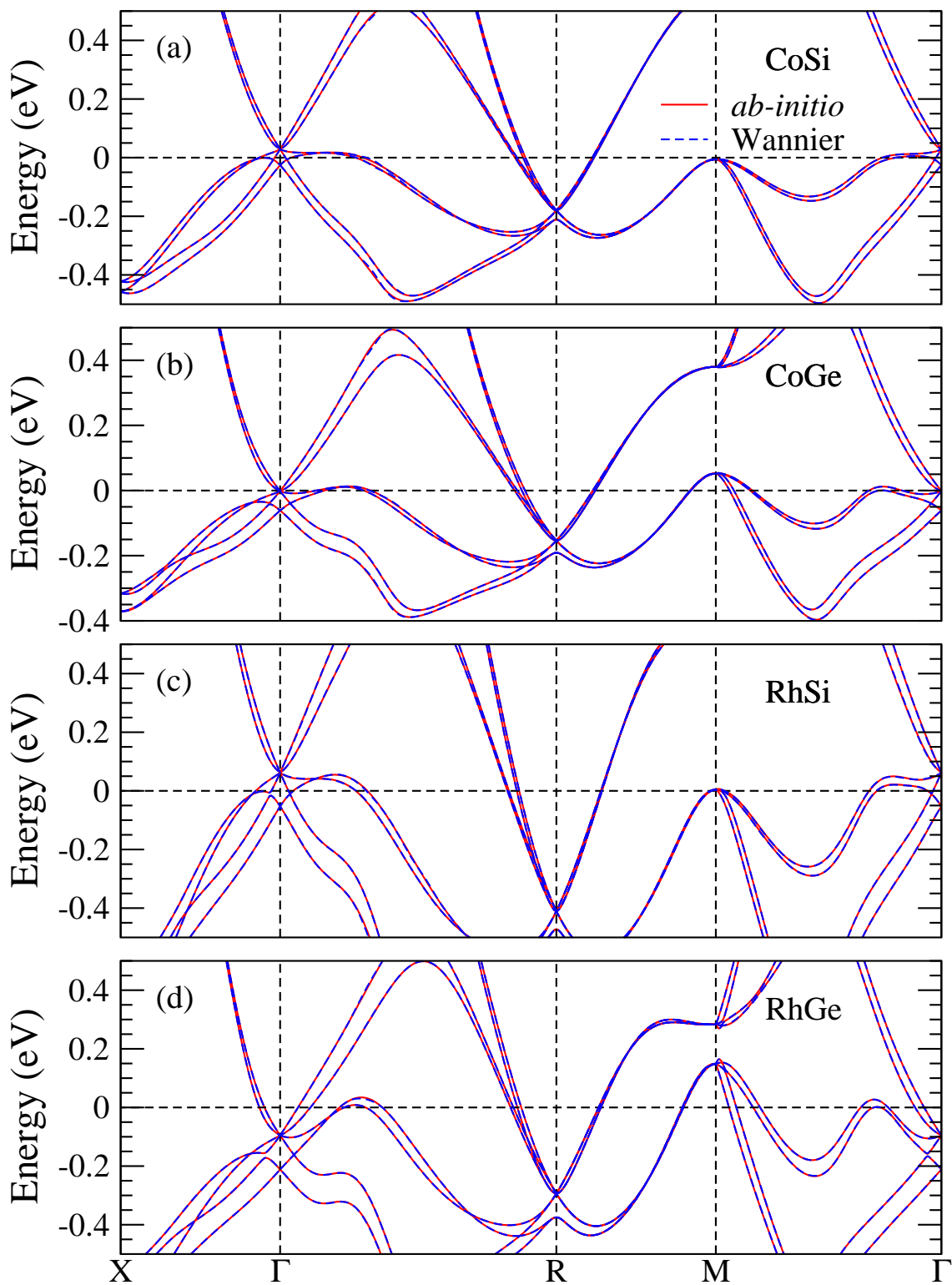


Figure 3.5: Band structure with SOC and maximally localized Wannier functions (MLWFs) of (a) CoSi, (b) CoGe, (c) RhSi, and (d) RhGe.  $E_F$  is at zero energy.

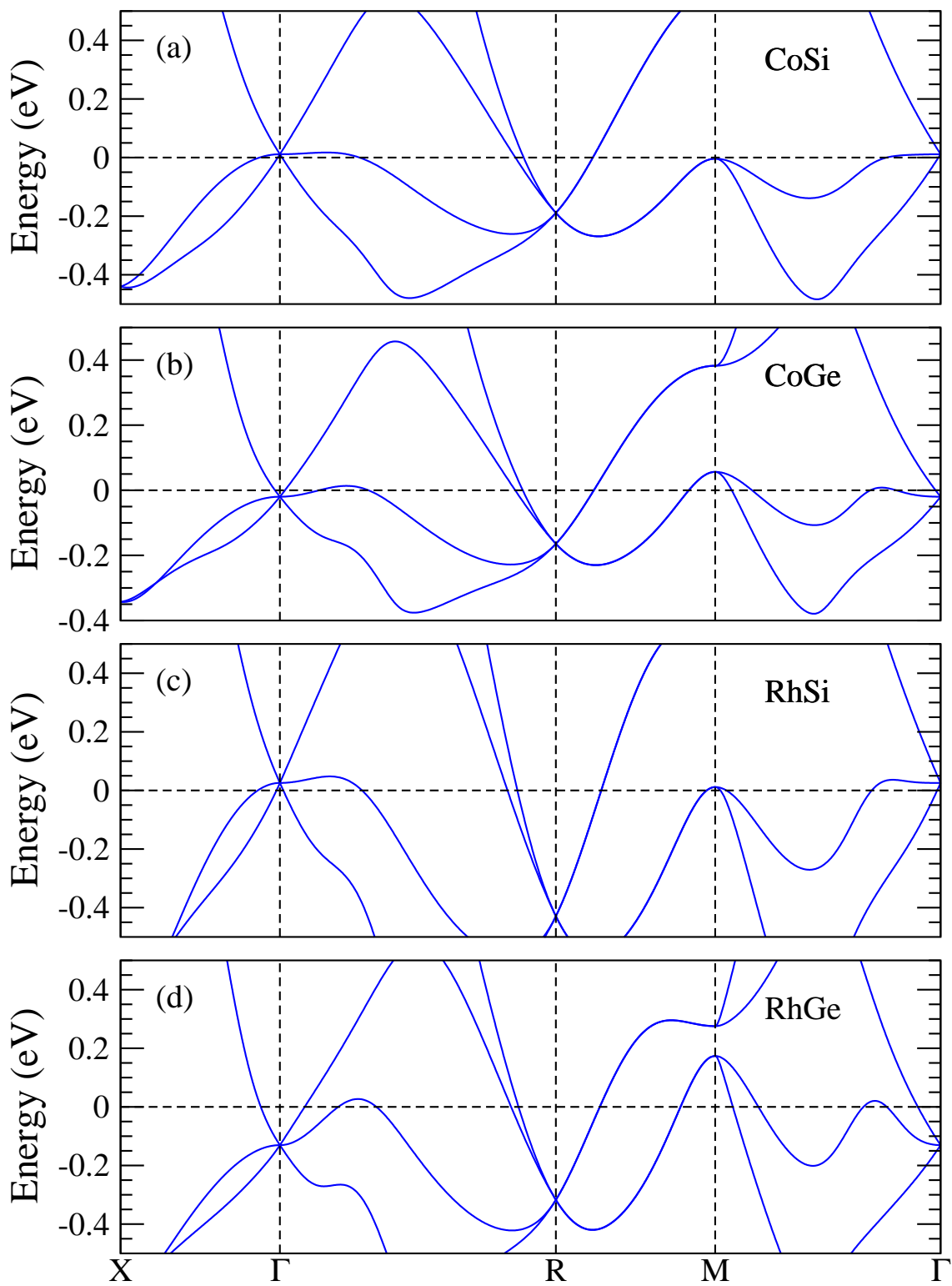


Figure 3.6: Band structure without SOC of (a) CoSi, (b) CoGe, (c) RhSi, and (d) RhGe.  $E_F$  is at zero energy.

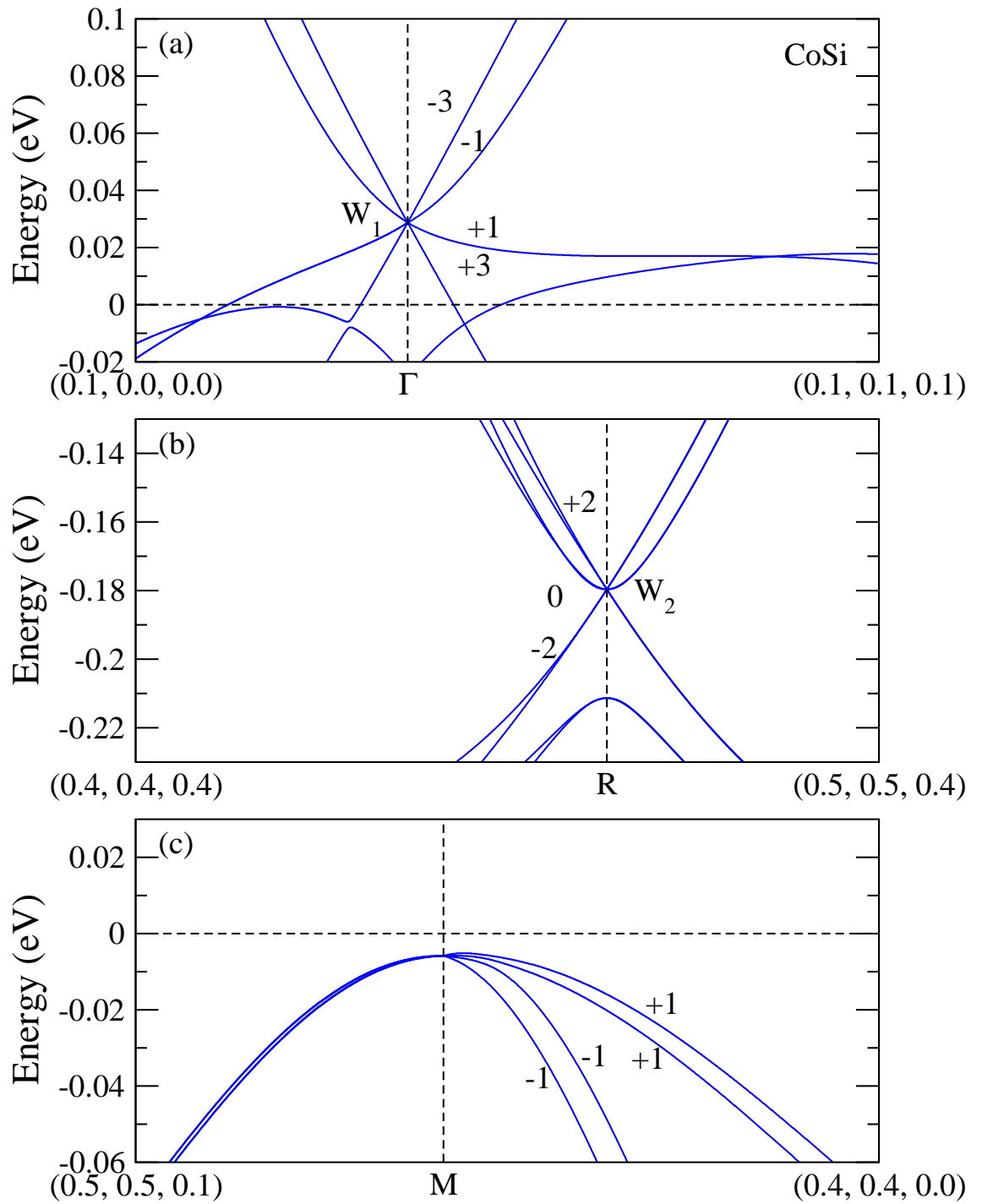


Figure 3.7: Bands structure with SOC of CoSi around (a)  $\Gamma$  point, (b)  $R$  point, (c)  $M$  point in the Brillouin zone. The number labeled in the plot means the band Chern numbers ( $C_b$ ), which was calculated by Wanniertools [43]. The Chern number  $C$  of the node is the sum over the occupied bands.

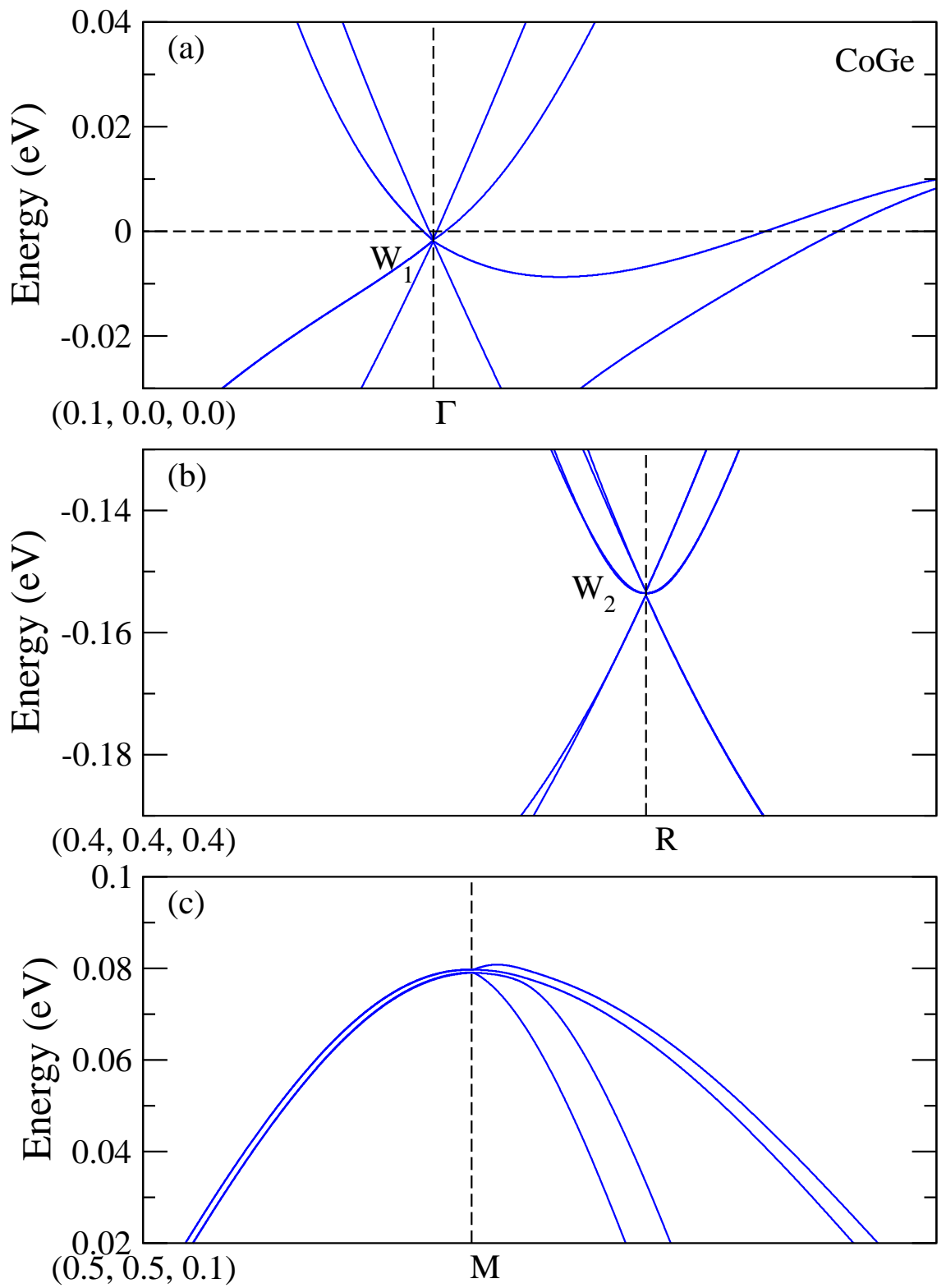


Figure 3.8: Bands structure with SOC of CoGe around (a)  $\Gamma$  point, (b)  $R$  point, (c)  $M$  point in the Brillouin zone.

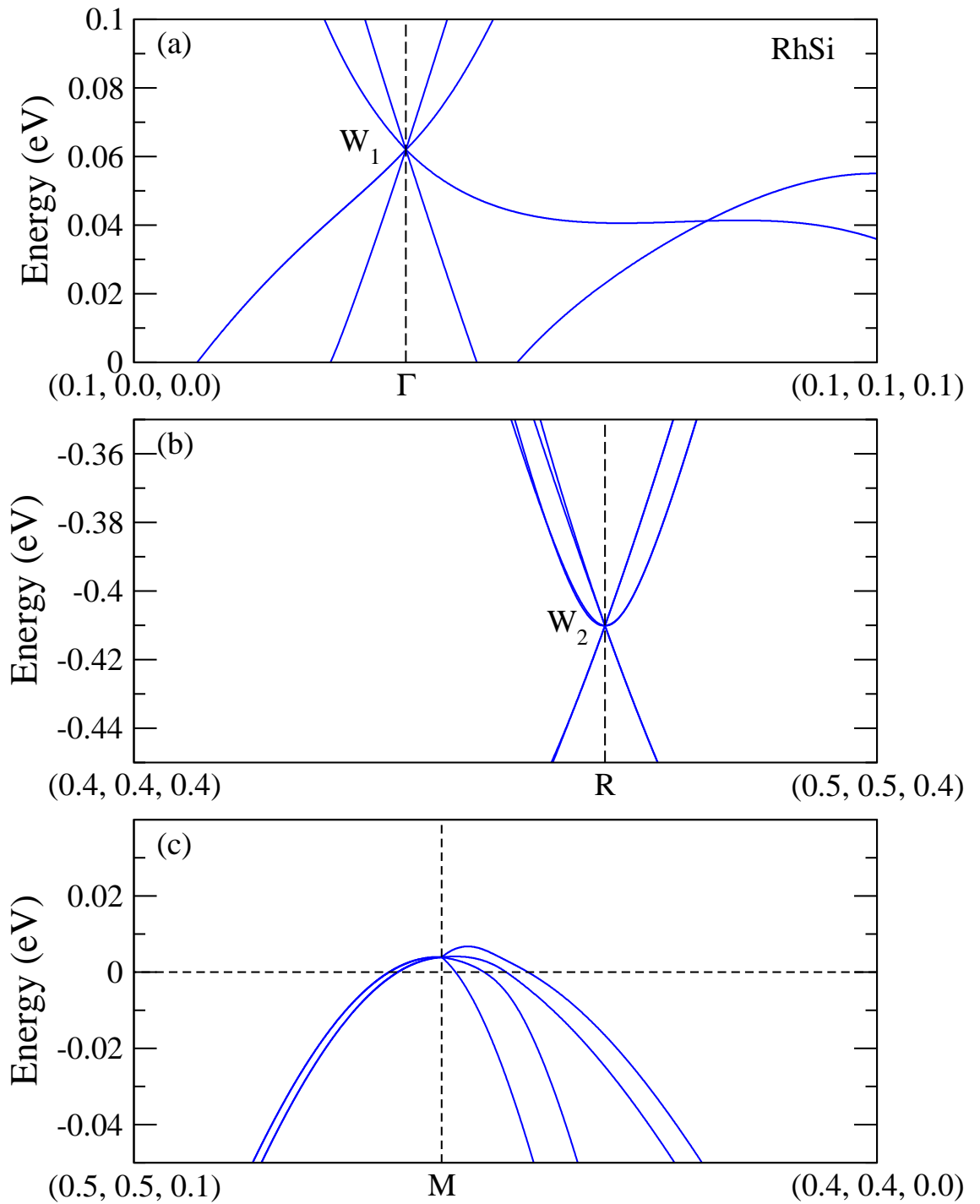


Figure 3.9: Bands structure with SOC of RhSi around (a)  $\Gamma$  point, (b)  $R$  point, (c)  $M$  point in the Brillouin zone.

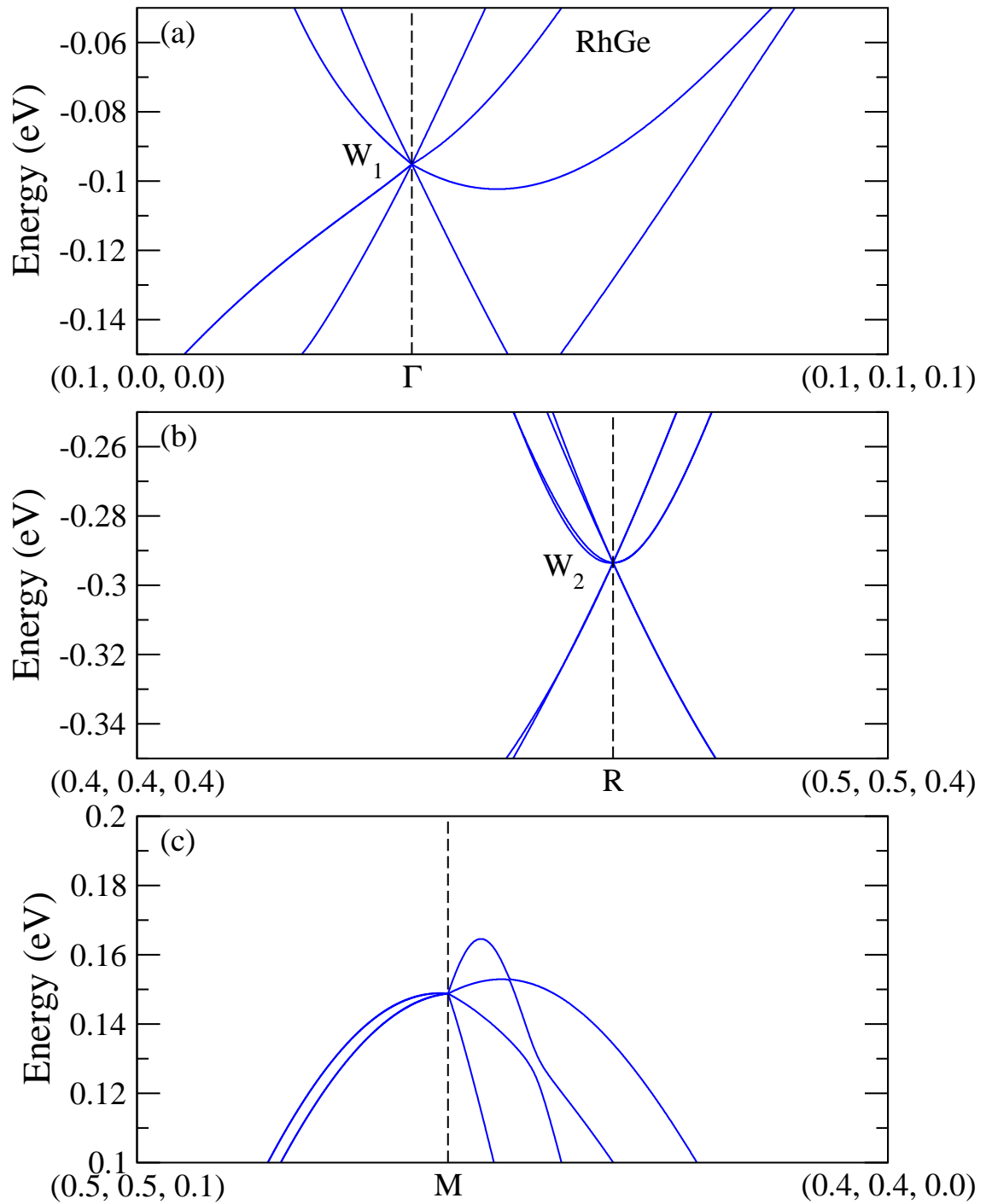


Figure 3.10: Bands structure with SOC of RhGe around (a)  $\Gamma$  point, (b)  $R$  point, (c)  $M$  point in the Brillouin zone.

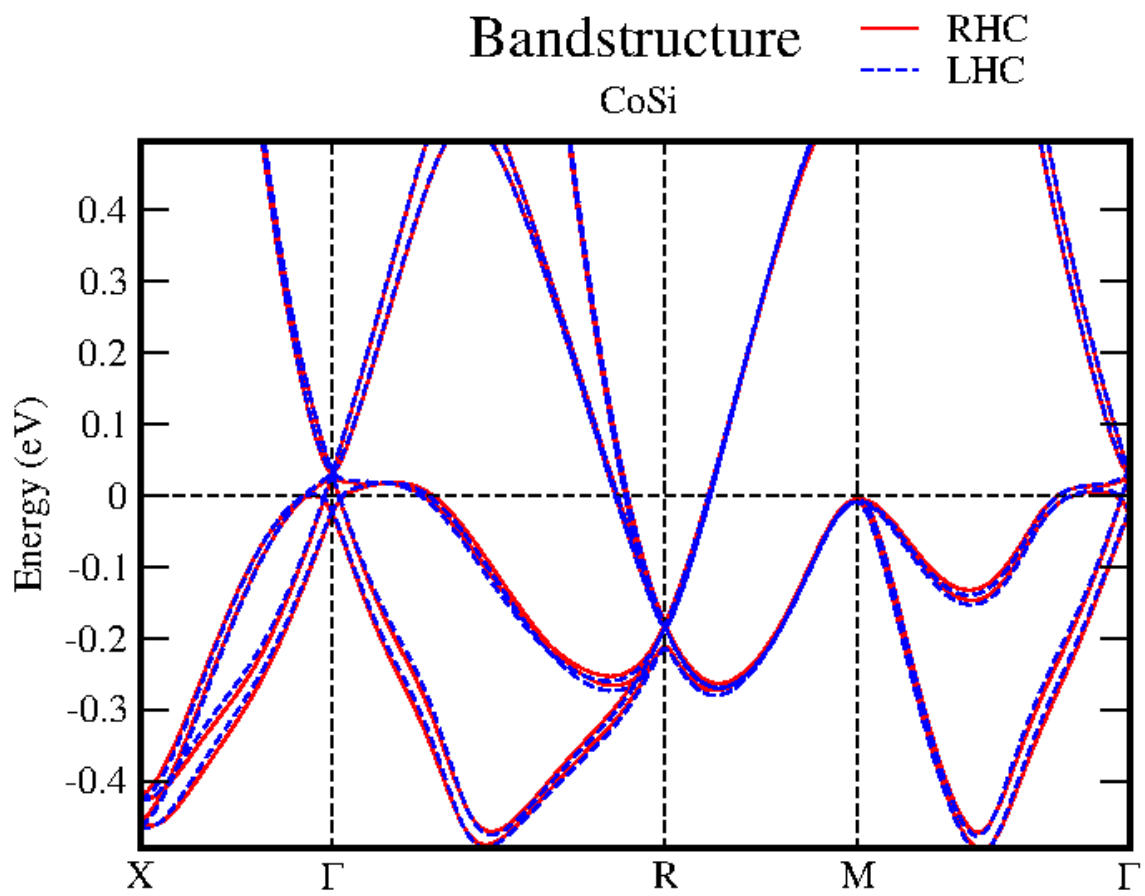


Figure 3.11: Band structure for RHC and LHC structure of CoSi.



## Chapter 4

# Spin Hall effect and spin Nernst effect in XY (X=Co, Rh; Y=Si, Ge)

### 4.1 Spin Hall effect

As mentioned in section 2.4, SHC is a third-rank tensor ( $\sigma_{ij}^k; i, j, k = x, y, z$ ). Thus, there are 27 possible nonzero tensor elements. However, because of the symmetry of the crystal, some of them would be prohibited or be the same as the other tensor elements. After checking the symmetry of space group  $P2_13$ , we figure out that there are only two independent tensor elements,  $\sigma_{xy}^z$  and  $\sigma_{yx}^z$  [44] for the material. The relation of the tensor elements is  $\sigma_{yz}^x = \sigma_{yx}^x = \sigma_{zx}^y$  and  $\sigma_{xz}^y = \sigma_{xy}^y = \sigma_{zy}^x$ , all the other tensor elements should be zero. Interestingly, for nonchiral cubic material Pt [27], there is only one independent tensor element  $\sigma_{xy}^z$ , and  $\sigma_{yx}^z = -\sigma_{xy}^z$ . This implies that due to the absence of chiral symmetry,  $\sigma_{yx}^z$  become an independent tensor element that doesn't have relation with  $\sigma_{xy}^z$ .

Moreover, since there are LHC and RHC for the chiral material, it's also important to know the SHC relation of both handedness. Because CoSi has experimental data for both RHC [33] and LHC [34] structures, we calculate the SHC for both structures in Fig. 4.1 and come to conclusion that  $\sigma_{xy}^z(LHC) \approx -\sigma_{yx}^z(RHC)$  and  $\sigma_{xz}^y(LHC) \approx -\sigma_{xy}^z(RHC)$ . The explicit relation is listed in Table 4.1. There are small differences between two results which are caused by atomic position difference of the experimental data. As a result, SHC

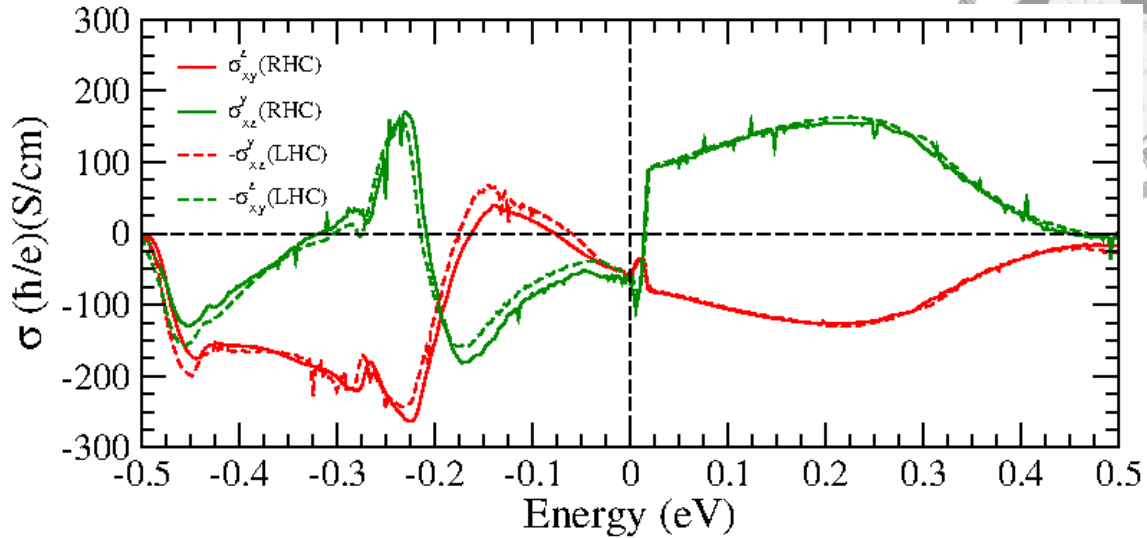
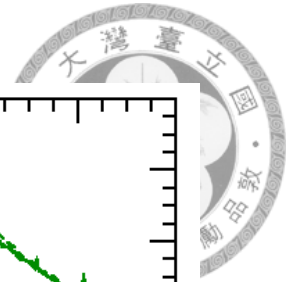


Figure 4.1: Calculated SHC ( $\sigma_{xy}^z$  and  $\sigma_{xz}^y$ ) for both RHC and LHC of CoSi.

can be used to identify the chirality of the structure, and this is also an interesting topic recently. However, the other three materials have only RHC structure. We'll focus on SHC of RHC structure in this thesis.

The SHC of the four compounds is listed in Table 4.2 with increasing order of SOC strength. For  $\sigma_{xy}^z$ , the value of CoSi is the smallest and RhGe is the largest which follows the strength order of SOC. However, the other tensor element  $\sigma_{xz}^y$  doesn't follow this trend. Also, the signs of  $\sigma_{xz}^y$  for RhSi and RhGe are different from CoSi and CoGe. Among these materials, the  $\sigma_{xy}^z$  of RhGe shows the largest SHC which is  $-139 (\hbar/e)(S/cm)$ . Compared with other representative materials, it's much smaller than Weyl semimetal TaAs [2] which has SHC of  $-781 (\hbar/e)(S/cm)$  and it's about 15 times smaller than Pt metal [27] whose SHC of  $-781 (\hbar/e)(S/cm)$ .

From Table 4.2 we can see that SHC of these materials show strong anisotropy. That is, after exchanging the electric field direction and the spin polarization direction SHC value can be pretty different. Take RhSi for example,  $\sigma_{xy}^z$ , which is under an electric field at  $y$  direction and spin polarize at  $z$  direction, is  $-122 (\hbar/e)(S/cm)$ . However, after changing electric field to  $z$  direction and spin polarize direction to  $y$  direction,  $\sigma_{xz}^y$  becomes  $11 (\hbar/e)(S/cm)$ , which is much smaller and the sign of SHC also changes.



$\underline{\sigma}^x$	SHC (RHC)			$\underline{\sigma}^x$	SHC (LHC)		
	$\underline{\sigma}^y$	$\underline{\sigma}^z$	$\underline{\sigma}^z$		$\underline{\sigma}^y$	$\underline{\sigma}^z$	
$\begin{pmatrix} 0 & 0 & 0 \\ 0 & 0 & \sigma_{xy}^z \\ 0 & \sigma_{xz}^y & 0 \end{pmatrix}$	$\begin{pmatrix} 0 & 0 & \sigma_{xz}^y \\ 0 & 0 & 0 \\ \sigma_{xy}^z & 0 & 0 \end{pmatrix}$	$\begin{pmatrix} 0 & \sigma_{xy}^z & 0 \\ \sigma_{xz}^y & 0 & 0 \\ 0 & 0 & 0 \end{pmatrix}$	$\begin{pmatrix} 0 & 0 & 0 \\ 0 & 0 & -\sigma_{xz}^y \\ 0 & -\sigma_{xy}^z & 0 \end{pmatrix}$	$\begin{pmatrix} 0 & 0 & -\sigma_{xy}^z \\ 0 & 0 & 0 \\ -\sigma_{xz}^y & 0 & 0 \end{pmatrix}$	$\begin{pmatrix} 0 & -\sigma_{xz}^y & 0 \\ -\sigma_{xy}^z & 0 & 0 \\ 0 & 0 & 0 \end{pmatrix}$		

Table 4.1: Tensor shape of SHC for  $P2_13$  space group with RHC and LHC, there are only two independent nonzero tensor elements  $\sigma_{xy}^z$  and  $\sigma_{xz}^y$ . Note that SNC has the same independent elements as SHC.

System	$\sigma_{xx}^c$ (S/cm)	$S_{xx}$ ( $\mu$ V/K)	$\sigma_{xy}^z$ ( $\hbar/e$ )(S/cm)	$\Theta_{sH}^z$ (%)	$\sigma_{xz}^y$ ( $\hbar/e$ )(S/cm)	$\Theta_{sH}^y$ (%)	$\alpha_{xy}^z$ ( $\hbar/e$ )(A/m K)	$\Theta_{sN}^z$ (%)	$\alpha_{xz}^y$ ( $\hbar/e$ )(A/m K)	$\Theta_{sN}^y$ (%)
CoSi	5200 <sup>c</sup>	-81 <sup>c</sup>	-63, 52 <sup>j</sup>	-2.4	-66	-2.5	0.42	-2.0	-1.00	4.7
CoGe	4589 <sup>d</sup>	-82 <sup>d</sup>	-131	-5.7	-21	-0.9	0.06	-0.3	-1.25	6.6
RhSi	3571 <sup>e</sup>	-25 <sup>h</sup>	-122	-6.8	11	0.6	0.14	-3.1	-0.65	-14.6
RhGe	4130 <sup>f</sup>	-25 <sup>f</sup>	-139	-6.7	103	5.0	0.64	-12.4	-0.19	-3.7
TaAs <sup>a</sup>	—	—	-781	—	-382	—	—	—	—	—
ZrSiS <sup>b</sup>	—	—	-79	—	-611	—	0.60	—	1.51	—
Pt	208333 <sup>g</sup>	-3.7 <sup>i</sup>	2139 <sup>m</sup>	10 <sup>g</sup>	—	—	-1.09 (-0.91) <sup>k</sup> , -1.57 <sup>i</sup>	-20 <sup>i</sup>	—	—

<sup>a</sup>*Ab initio* calculation [2]; <sup>b</sup>*Ab initio* calculation [4]; <sup>c</sup>Transport experiment [45]; <sup>d</sup>Transport experiment [46]; <sup>e</sup>Transport experiment [47]; <sup>f</sup>Transport experiment [48]; <sup>g</sup>Transport experiment [49]; <sup>h</sup>Assumed the same value as RhGe from [48]; <sup>i</sup>Experiment at 255 K [52]; <sup>j</sup>*Ab initio* calculation [51]; <sup>m</sup>*Ab initio* calculation [27].

Table 4.2: Calculated SHC and SNC at  $T = 300K$  for all four CoSi family materials. SHC and SNC from previously studied Weyl semimetal TaAs, Dirac semimetal ZrSiS, and transition metal Pt are also in the list. We also show the experimental measurement of electrical conductivity  $\sigma_{xx}^c$  and Seeback coefficient  $S_{xx}$  used for calculating spin Hall angle  $\Theta_{sH}$  and spin Nernst angle  $\Theta_{sN}$ .



System	$E(W_1)$ (eV)	$E(W_2)$ (eV)	$E(W_3)$ (eV)	$\sigma_{xy}^z$ ( $\hbar/e$ )(S/cm)	$\sigma_{xz}^y$ ( $\hbar/e$ )(S/cm)	$\alpha_{xy}^z$ ( $\hbar/e$ )(A/m K)	$\alpha_{xz}^y$ ( $\hbar/e$ )(A/m K)
CoSi	0.028	-0.180	-0.026	-83 (-54)	93 (-166)	0.39 (-1.35)	-1.07 (1.05)
CoGe	-0.002	-0.154	-0.062	-139 (-130)	-38 (-98)	0.07 (-1.12)	-1.24 (0.74)
RhSi	0.062	-0.410	-0.053	-89 (-92)	114 (-179)	-0.02 (-0.88)	-0.52 (1.24)
RhGe	-0.096	-0.294	-0.212	-198 (-118)	103 (-24)	0.22 (-0.70)	-0.26 (0.20)

Table 4.3: Energy levels of Weyl fermion nodes  $W_1$ ,  $W_2$ , and  $W_3$  for each materials. SHC ( $\sigma_{xy}^z$  and  $\sigma_{xz}^y$ ) and SNC ( $\alpha_{xy}^z$  and  $\alpha_{xz}^y$ ) at  $T = 300K$  after shifting  $\mu$  to  $W_1$  and  $W_2$  are also listed in the table. Note that the values in the parentheses mean  $\mu = W_2$ .

Since the multifold fermion nodes  $W_1$  and  $W_2$  are not located exactly at  $E_F$ , we also calculate SHC as a function of  $E_F$  with rigid-band approximation which assumes that changing the chemical potential  $\mu$  won't change the band structure. The results are shown in Figs. 4.2 and 4.3, and the exact SHC values of shifting  $\mu$  to  $W_1$  and  $W_2$  are also listed in Table 4.3. From the spectrum of SHC, it's obvious that SHC has a strong dependence on  $\mu$ , especially near  $W_1$  for both CoSi and CoGe. The value of  $\sigma_{xz}^y$  of CoSi changes dramatically between  $E_F$  and  $W_1$ . When it is at  $E_F$   $\sigma_{xz}^y$  is -63 ( $\hbar/e$ )(S/cm). However, when  $\mu$  is shifted to above  $E_F$ ,  $\sigma_{xz}^y$  keeps increasing and changing sign, and finally reaching 93 ( $\hbar/e$ )(S/cm) when  $\mu$  is shifted to  $W_1$ , which is only 0.0028 eV above  $E_F$ . Similarly,  $\sigma_{xz}^y$  also changes rapidly between  $E_F$  and  $W_1$ . Moreover, the feature of rapid changing SHC can also be found when  $\mu$  is shifted further to  $W_2$ . Nonetheless, this feature seems to only exist in  $\sigma_{xz}^y$ . The other component  $\sigma_{xy}^z$  is smoother compared to  $\sigma_{xz}^y$ .

Besides the rapidly changing SHC feature mentioned above, there are still some other noticeable features for SHC.  $\sigma_{xz}^y$  of RhSi increases from 11 ( $\hbar/e$ )(S/cm) to 114 ( $\hbar/e$ )(S/cm) by raising  $\mu$  a little bit to  $W_1$  at 0.06 meV above  $E_F$ , which can be realized with electron doping of 0.02 e/f.u.  $\sigma_{xz}^y$  of CoGe also change from -21 ( $\hbar/e$ )(S/cm) to -98 ( $\hbar/e$ )(S/cm) through shifting  $\mu$  to  $W_2$  at -0.15 eV below  $E_F$  with -0.27 e/f.u. hole doping. Both  $\sigma_{xy}^z$  of CoGe and RhGe has a large value of -260 ( $\hbar/e$ )(S/cm) and -202 ( $\hbar/e$ )(S/cm) by shifting to -0.19 eV and -0.07 eV below  $E_F$  with 0.38 e/f.u. and 0.04 e/f.u. hole doping, respectively. The results suggest that SHC value can increase dramatically with electron or hole doping.

Until now, the only material among the CoSi family that has been studied for SHC



is CoSi by Tang *et al.* [12]. They measure SHC of CoSi with CoSi/CoFeB/MgO heterostructure and came out the damping like ( $\sigma_{DL}$ ) SHC for film with thickness  $t_{CoSi}=7.2$  nm was  $45 (\hbar/e)(S/cm)$ , and fieldlike ( $\sigma_{FL}$ ) is  $95 (\hbar/e)(S/cm)$ . They also performed DFT calculation and got  $\sigma_{xy}^z=52 (\hbar/e)(S/cm)$ . These results are close to our calculation listed in Table 4.2. However, the spectrum of their paper seems to be more similar to  $\sigma_{xz}^y$  of Fig. 4.2(b) except for the sign difference. That is,  $\sigma_{xy}^z$  [12]  $\approx -\sigma_{xz}^y$  [this work], which implies that they should have a LHC structure. Also notice that they only studied one component which was  $\sigma_{xy}^z$ .  $\sigma_{xz}^y$  was not considered in their paper.

Another important quantity that needs to take into account in the application of SHE is the spin Hall angle ( $\Theta_{sH}$ ).  $\Theta_{sH}$  can be easily calculated by  $\Theta_{sH} = (2e/\hbar)J^s/J^c = 2\sigma^s/\sigma^c$ , where  $J^c$  and  $\sigma^c$  represent longitudinal charge current density as well as conductivity. Even though Pt metal has the largest SHC among all transition metals, its metallic nature makes it also have a large conductivity, which reduces its  $\Theta_{sH}$ . On the other hand, Weyl semimetals have a much smaller conductivity so that even with smaller SHC they might have a larger  $\Theta_{sH}$ . We list all the  $\Theta_{sH}$  of the CoSi family in Table 4.2, and we find that  $\Theta_{sH}^z$  of RhGe and RhSi are almost -7% which are close to 10% of Pt metal.

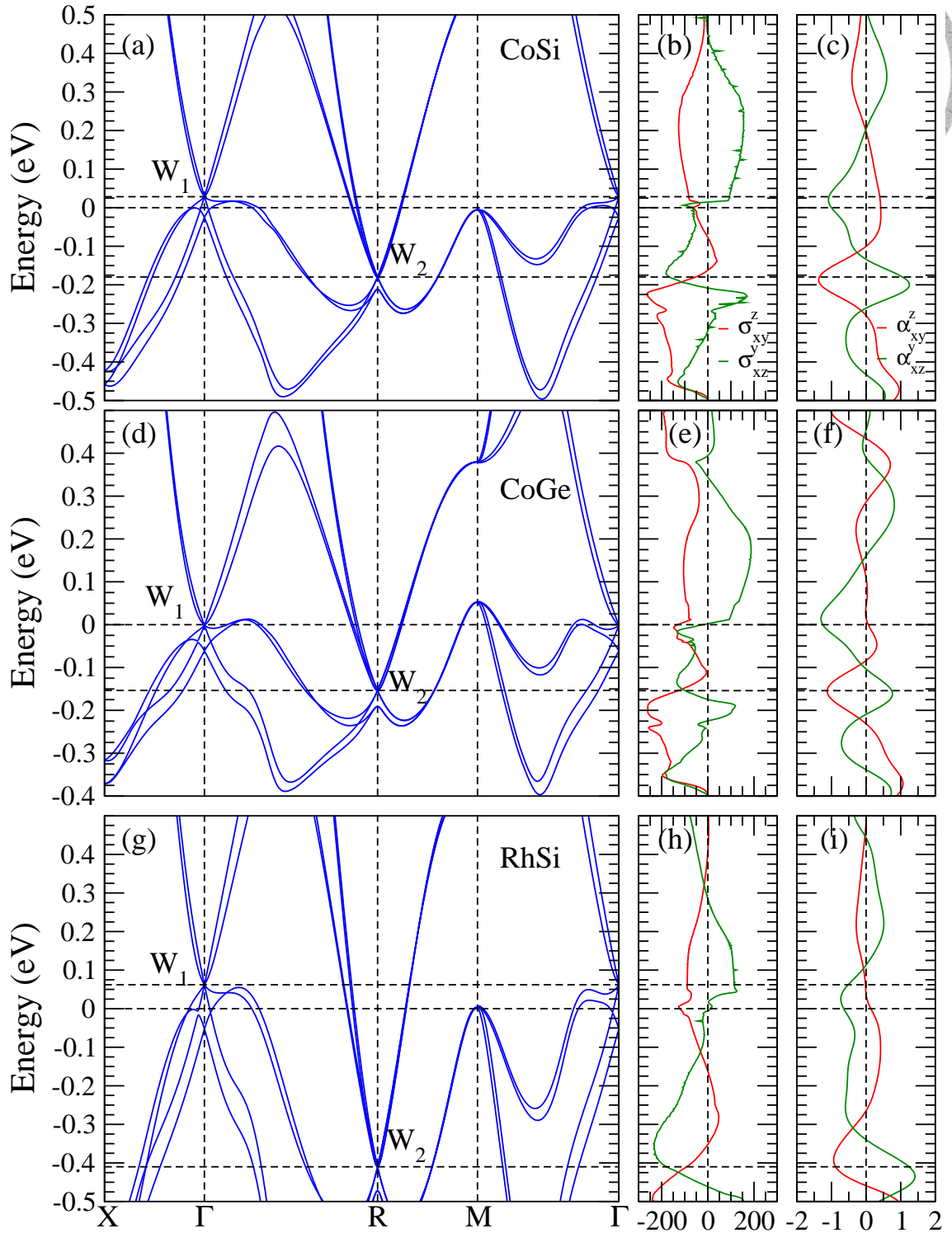


Figure 4.2: (a, d, g) Band structure with SOC, (b, e, h) SHC ( $\sigma_{xy}^z$  and  $\sigma_{xz}^y$ ) as a function of  $\mu$ , and (c, f, i) SNC ( $\alpha_{xy}^z$  and  $\alpha_{xz}^y$ ) as a function of  $\mu$  for CoSi (a, b, c), CoGe (d, e, f) and RhSi (i, j, k), respectively.  $E_F$  is at zero energy.

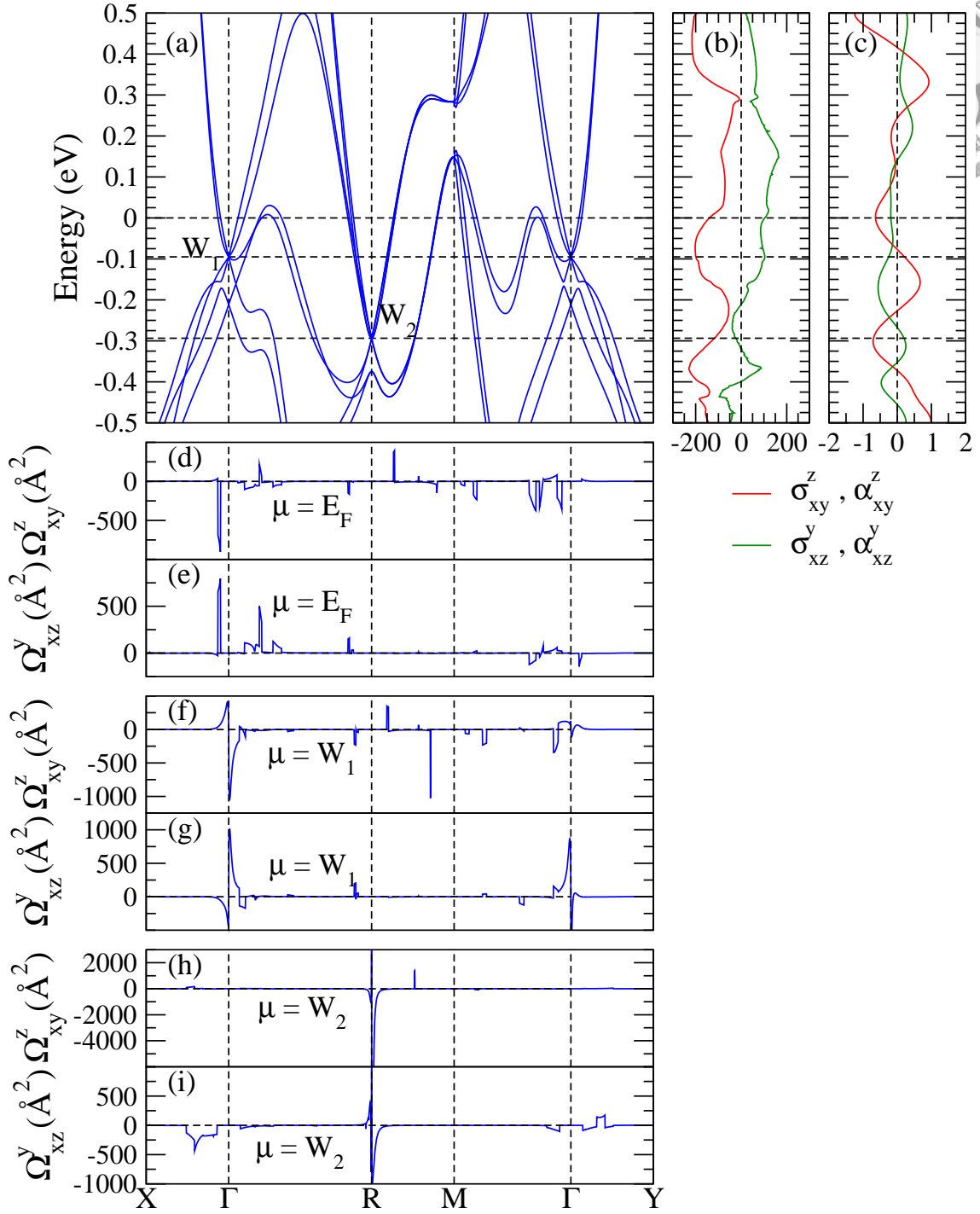


Figure 4.3: (a) Band structure with SOC, (b) SHC ( $\sigma_{xy}^z$  and  $\sigma_{xz}^y$ ) as a function of  $\mu$ , and (c) SNC ( $\alpha_{xy}^z$  and  $\alpha_{xz}^y$ ) as a function of  $\mu$  for RhGe. (d, f, h) is SBC  $\Omega_{xy}^z$  and (e, g, i) is SBC  $\Omega_{xz}^y$  for  $\mu = E_F$ ,  $\mu = W_1$ , and  $\mu = W_2$ , respectively.  $E_F$  is at zero energy.

## 4.2 Spin Nernst effect

Similar to SHC, SNC tensor ( $\alpha_{ij}^k; i, j, k = x, y, z$ ) is also a third-rank tensor with 27 elements. However, by considering symmetry they reduce to only two independent tensor



elements  $\alpha_{xy}^z$  and  $\alpha_{xz}^y$  [44]. The calculated SNC at  $T = 300K$  of the CoSi family also listed in Table 4.2. Interestingly, among four materials,  $\alpha_{xz}^y$  of CoSi and CoGe are large with values  $-1.00$  ( $\hbar/e$ )(A/m K) and  $-1.25$  ( $\hbar/e$ )(A/m K), respectively. It's comparable to  $\alpha_{xy}^z$  of Pt metal in Table 4.2 and recently reported Dirac-semimetal ZrSiS [4]. Even having a much smaller SHC compared to Pt and ZrSiS, the CoSi family seems to have a good SNC value and can potentially be used in spin caloritronics.

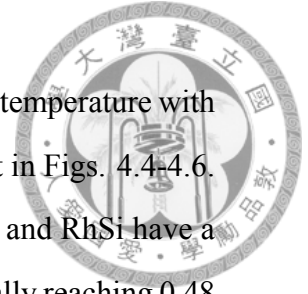
SNC tensor elements of the CoSi family have a strong anisotropic feature as well. Take CoGe as an example, when having the electric field in the  $y$  direction and spin polarization in the  $z$  direction,  $\alpha_{xz}^y$  is only  $0.06$  ( $\hbar/e$ )(A/m K), which is way smaller than  $\alpha_{xz}^y = -1.25$  ( $\hbar/e$ )(A/m K) mentioned above and the sign of it also becomes different. A similar feature can also be found in the other three materials.

To get more insight into SNC, we also do the calculation as a function of  $E_F$  for SNC at  $T = 300K$  [See Figs. 4.2 and 4.3]. The values after shifting  $\mu$  to  $W_1$  and  $W_2$  are also listed in Table 4.3. Just like the SHC spectrum, SNC also changes a lot by shifting  $\mu$ , especially shifting it to  $W_2$ . For example,  $\alpha_{xz}^y$  of CoGe becomes  $-1.12$  ( $\hbar/e$ )(A/m K) after shifting  $\mu$  to  $W_2$  which is  $-0.15$  eV below  $E_F$  and can be realized by hole doping  $0.27$  e/f.u.  $\alpha_{xy}^z$  of CoSi also enhances from  $0.42$  ( $\hbar/e$ )(A/m K) to  $-1.35$  ( $\hbar/e$ )(A/m K) after shifting to  $W_2$  located at  $-0.18$  eV with  $0.25$  eV hole doping. Besides shifting  $\mu$  to  $W_2$ ,  $\alpha_{xy}^z$  of RhGe also increases from  $-0.19$  ( $\hbar/e$ )(A/m K) to  $-0.26$  ( $\hbar/e$ )(A/m K) after shifting  $\mu$  to  $W_1$  with  $0.06$  e/f.u. electron doping.

For SNC in low temperature limit, there's an equation called Mott [29] relation that can help us understand the relation between SHC and SNC quite well. That is

$$\alpha_{ij}^s(E_F) = -\frac{\pi^2 k_B^2 T}{3e} \sigma_{ij}^s(E_F)'. \quad (4.1)$$

From the Mott relation, we can easily conclude that SNC is proportional to the derivative of SHC in the low temperature limit at a certain energy  $\mu$ . This can explain why  $\alpha_{xz}^y$  of CoSi and CoGe are large around  $E_F$  since  $\sigma_{xz}^y$  for both of them show a steep slope between  $E_F$  and  $W_1$ . And the enhanced SNC around  $W_2$  can also be explained by rapid change of the SHC around  $W_2$  for the CoSi family.



On the other hand, we also do the calculation of SNC as a function of temperature with the chemical potential being at  $E_F$ ,  $W_1$ , and  $W_2$ , respectively, and plot it in Figs. 4.4-4.6. When  $\mu=E_F$  and the temperature is higher than 60 K,  $\alpha_{xz}^y$  of both CoSi and RhSi have a positive SNC.  $\alpha_{xy}^z$  keeps increasing as the temperature increases, and finally reaching 0.48  $(\hbar/e)(A/m K)$  and 0.20  $(\hbar/e)(A/m K)$  at 400 K, respectively. In contrast,  $\alpha_{xy}^z$  of RhGe is always negative. For  $\alpha_{xz}^y$ , it seems that all materials have a negative SNC and increase their values as the temperature increases.  $\alpha_{xz}^y$  of CoSi, RhSi, CoGe, and RhGe finally reach -1.12, -1.30, -0.73 and -0.24  $(\hbar/e)(A/m K)$  at 400K, respectively.

In the end, the spin Nernst angle ( $\Theta_{sN}$ ) which is important for the application of spin caloritronics is also listed in Table 4.2. The definition of it is  $\Theta_{sN} = (2e/\hbar)J^s/J^h = 2\alpha^s/\alpha^L$ , where  $J^s$  is heat current density and  $\alpha^L$  is Nernst coefficient [50]. We use the data of Seebeck coefficient ( $S_{xx}$ ) to estimate  $\alpha^L$  with the relation that  $\alpha^L = S_{xx}\sigma_{xx}$ . Among them,  $\Theta_{sN}^z$  of RhGe and  $\Theta_{sN}^y$  of RhSi are -12.4% and -14.6%, respectively, which is comparable to 20% [50] of Pt metal. Up to now, there isn't any study about the SNE of the CoSi family. With the large  $\Theta_{sN}$  of RhSi and RhGe, hopefully, there will be more studies about this topic in the near future.

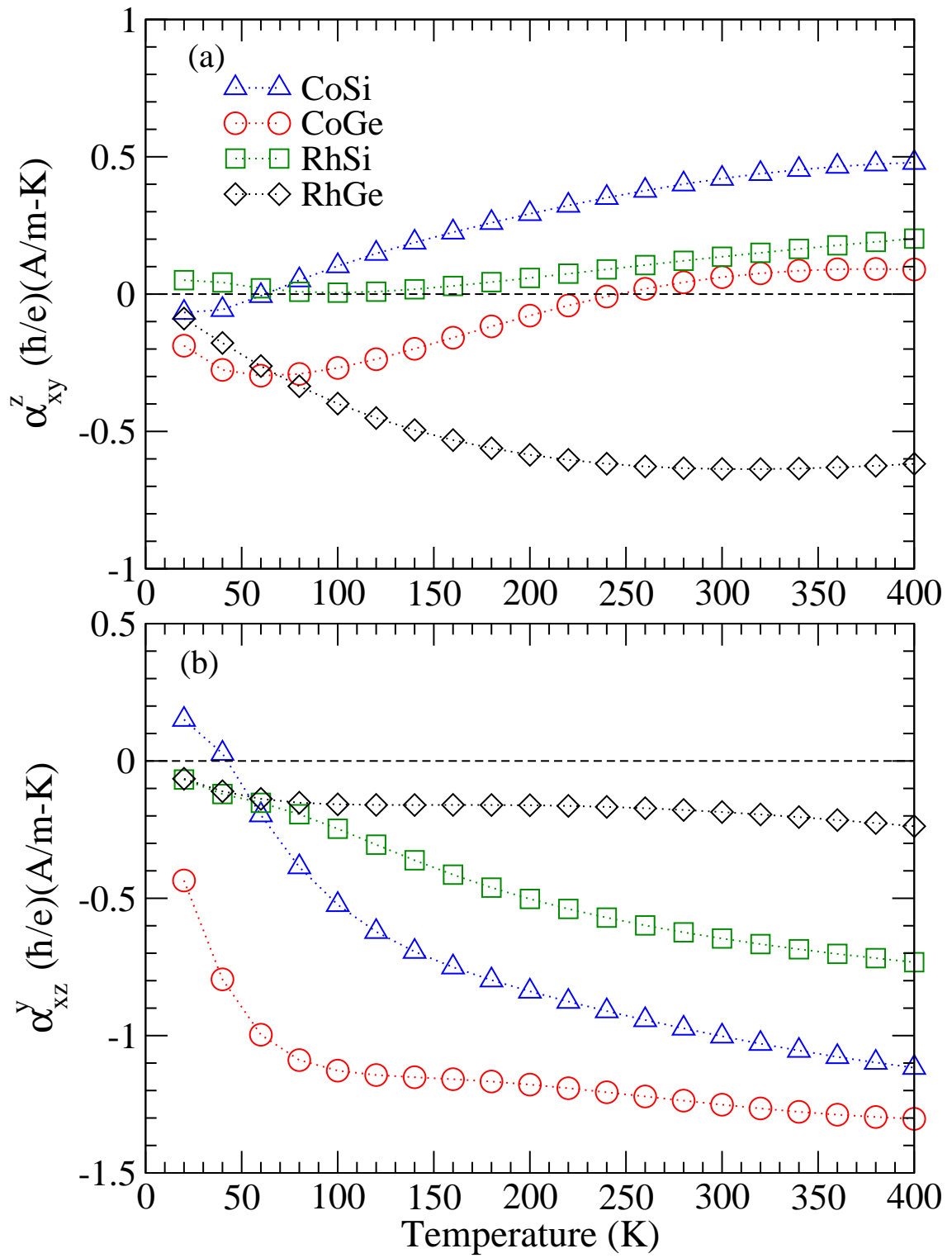


Figure 4.4: SNC of CoSi family (a)  $\alpha_{xy}^z$  and (b)  $\alpha_{xz}^y$  as a function of temperature  $T$  when  $\mu = E_F$ .

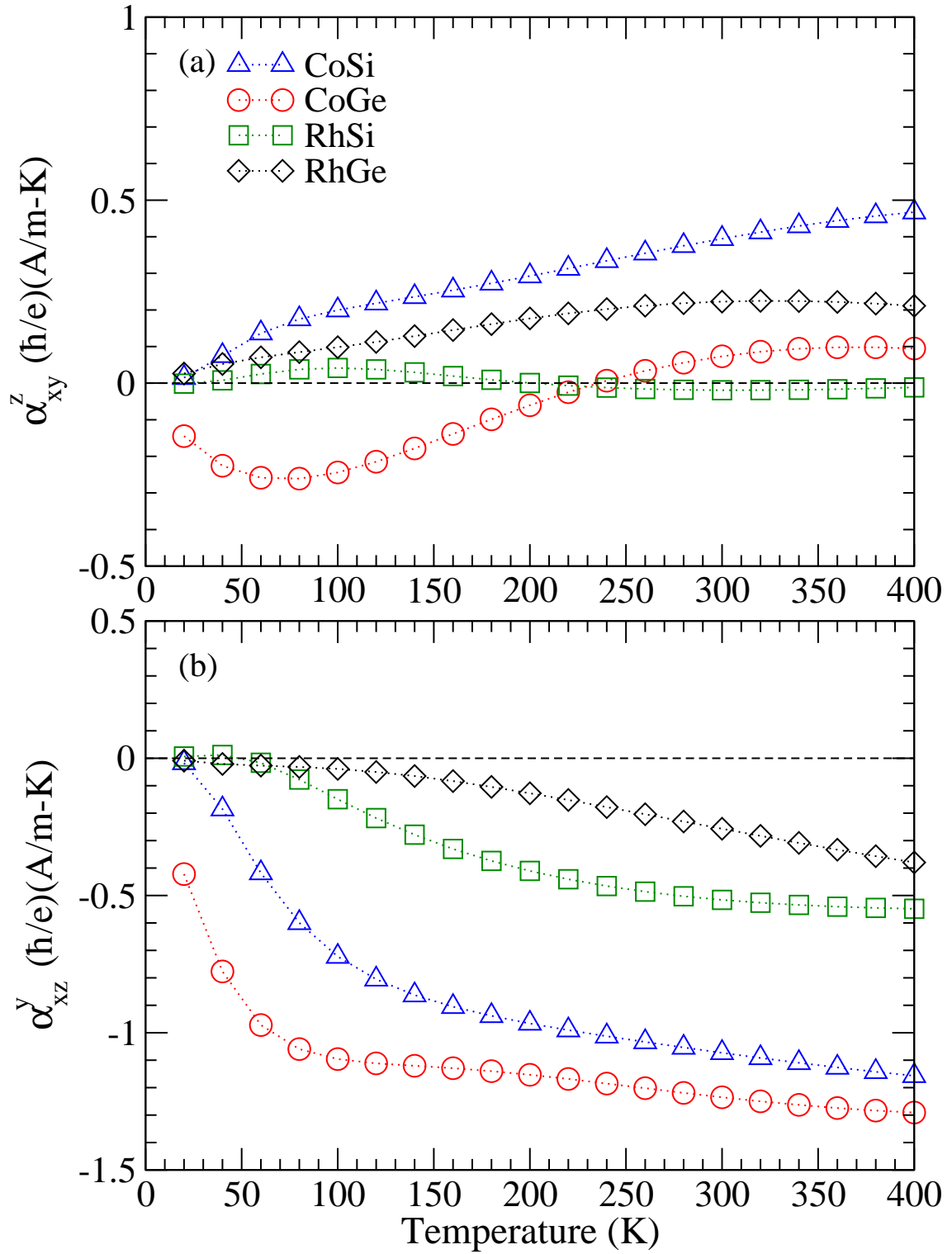


Figure 4.5: SNC of CoSi family (a)  $\alpha_{xy}^z$  and (b)  $\alpha_{xz}^y$  as a function of temperature  $T$  when  $\mu = W_1$ .

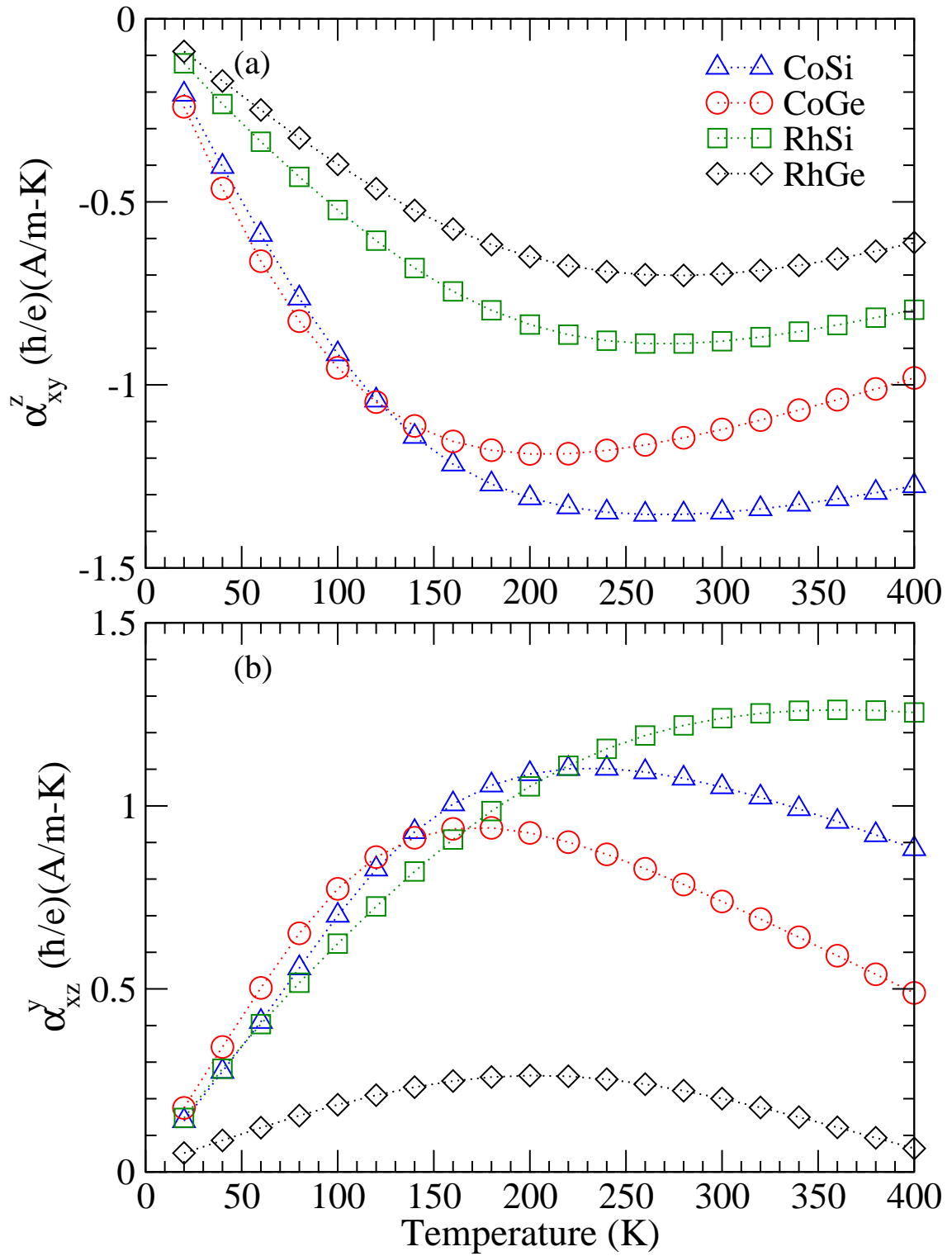


Figure 4.6: SNC of CoSi family (a)  $\alpha_{xy}^z$  and (b)  $\alpha_{xz}^y$  as a function of temperature  $T$  when  $\mu = W_2$ .



### 4.3 Spin Berry curvature analysis

From Eqs. (2.12) and (2.13) for the SHC, it's easy to know that SBC is one of the dominant contributions to SHC. As a result, it's important to look at the SBC of the materials to know the origin of SHC. Since RhGe has the largest SHC among the materials, we take it as an example to show how SBC works in the CoSi family. We plot the SBC along high-symmetry lines for  $\mu$  equal to  $E_F$ ,  $W_1$  and,  $W_2$ , respectively [see Fig. 4.3]. Also, to make it clearer we make contour plots as well in Figs. 4.7 and 4.8. Panels (a), (b) and (c) are on the  $k_x k_y$  plane with  $k_z = 0$  when  $\mu = E_F$ ,  $\mu = W_1$ , and  $\mu = W_2$ , respectively. And panel (d) is on the  $k_x k_z$  plane with  $k_y = 0.5$  to include the contribution from  $R$  point.

For  $\mu = E_F$ ,  $\sigma_{xy}^z$ , and  $\sigma_{xz}^y$  of RhGe are positive and negative, respectively. From Fig. 4.3, we can figure out this is mainly due to the large positive peak of  $\Omega_{xy}^z$  and negative peak of  $\Omega_{xz}^y$  along the  $X - \Gamma$  line. From previous studies [27] we know that when degenerate bands are splitted by SOC, they produce large SBC around that region with opposite signs. If both bands are occupied, the large peaks of the opposite signs will cancel each other. Nonetheless, when  $E_F$  is located between these two bands, only the lower one contributes to the SBC and thus generates SHC. This may be the reason why there's a peak along the  $X - \Gamma$  line. Moreover, with the contour plots [see Figs. 4.7 and 4.8] we further confirm that besides along  $X - \Gamma$ ,  $\Gamma - R$  also contributes to the SHC.

When lowering  $\mu$  to  $W_1$ , we can see that there is an asymmetric peak around the  $\Gamma$  point in Fig. 4.3. This asymmetric peak also appears at the  $R$  point when shifting  $\mu$  to  $W_2$ . Consequently, perhaps it's the trait of the multifold Weyl node. The peak of  $\Omega_{xy}^z$  along  $\Gamma - R$  seems to be more predominant than the one along  $X - \Gamma$  and thus leads to negative SHC. A similar claim can be made for  $\Omega_{xz}^y$ , in which the peak mainly comes from  $\Gamma - R$  and  $M - \Gamma$  line. For  $\mu = W_2$ , the predominant peak is along the  $R - M$  line for both  $\Omega_{xy}^z$  and  $\Omega_{xz}^y$ , and also a little bit comes from  $k_x k_y$  plane. Therefore, this leads to negative SHC for both  $\Omega_{xy}^z$  and  $\Omega_{xz}^y$ .

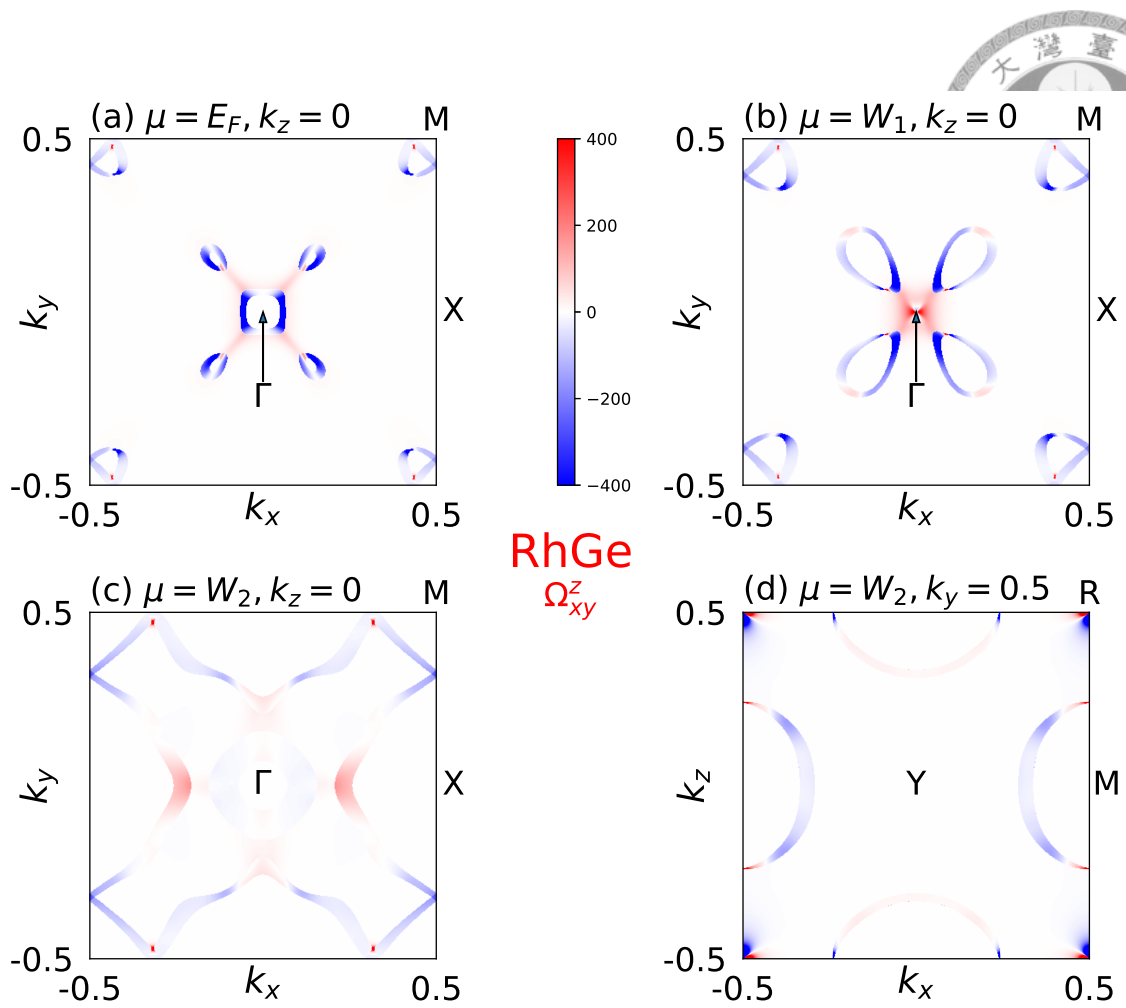


Figure 4.7: SBC  $\Omega_{xy}^z$  contour plot for RhGe at  $k_x k_y$  plane with  $k_z = 0$  when (a)  $\mu = E_F$ , (b)  $\mu = W_1$ , and (c)  $\mu = W_2$ . (d)  $\Omega_{xy}^z$  contour plot for  $k_x k_z$  plane with  $k_y = 0.5$  when  $\mu = W_2$ .

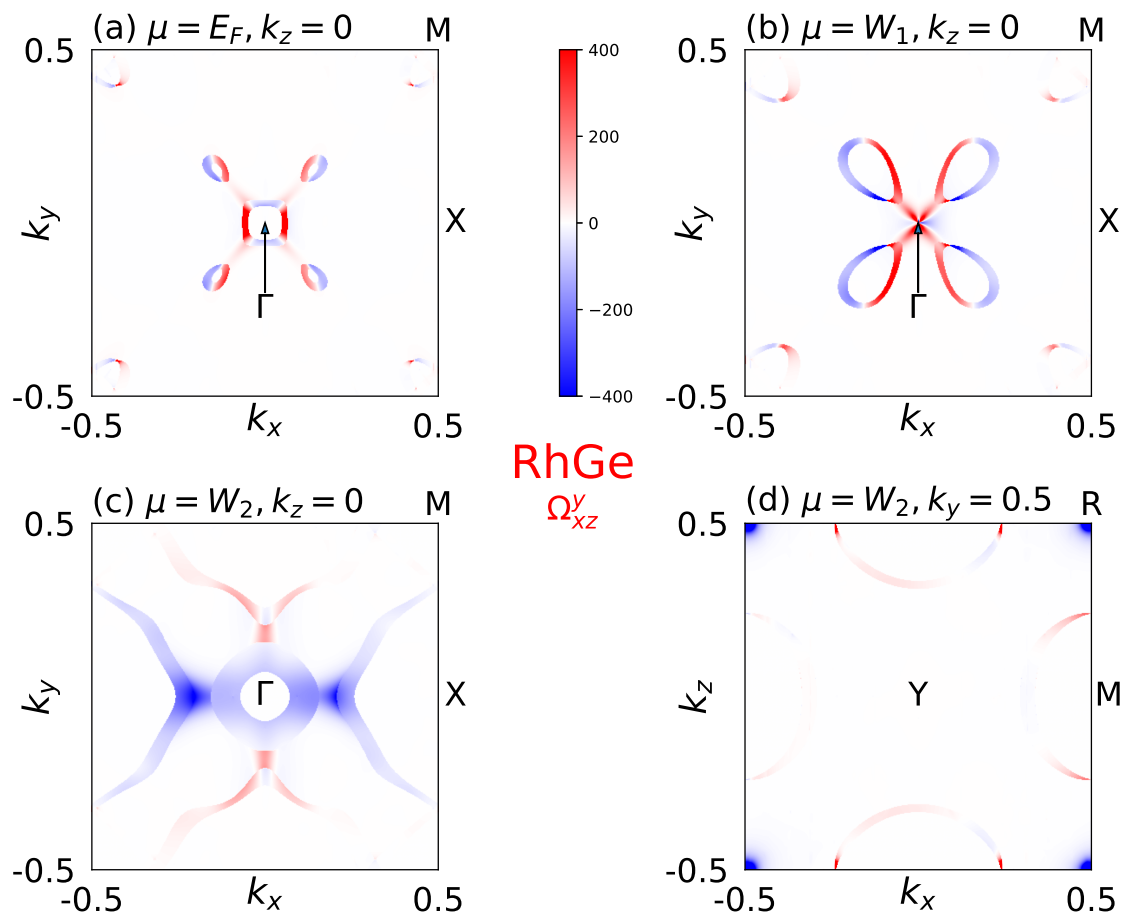


Figure 4.8: SBC  $\Omega_{xz}^y$  contour plot for RhGe at  $k_x k_y$  plane with  $k_z = 0$  when (a)  $\mu = E_F$ , (b)  $\mu = W_1$  and (c)  $\mu = W_2$ . (d)  $\Omega_{xz}^y$  contour plot for  $k_x k_z$  plane with  $k_y = 0.5$  when  $\mu = W_2$ .





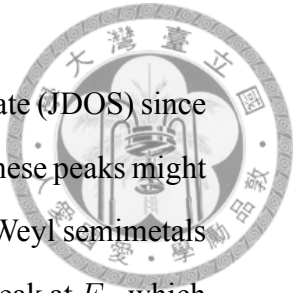
## Chapter 5

# Nonlinear optical effects in XY (X=Co, Rh; Y=Si, Ge)

### 5.1 Bulk photovoltaic effect

As mentioned earlier in section 2.5, BPVE includes linear part and circular part of the shift and injection current. However, we can simplify it with the symmetry of the crystal [32]. In our cases, the CoSi family has time-reversal symmetry and lacks  $PT$  symmetry. As a result, both circular shift current and linear injection current should vanish. In this section, we calculate the linear shift current and circular injection current for the CoSi family in low frequency region using different smearing factors  $\eta$ , which is 10 meV (normal smearing factor for Weyl semimetal), 38 meV (smearing factor reported for CoSi [14]), 100 meV (smearing factor reported for RhSi [14]). And the optical conductivity is calculated with the smearing factor 10 meV. The smearing factor is related to material hot-carrier lifetime ( $\tau$ ) with relation  $\hbar/\tau = \eta$ .

For the linear shift current, the only independent conductivity tensor element for CoSi family is  $\sigma_{xyz} = \sigma_{yzx} = \sigma_{zxy}$  [44]. The calculated results are shown in the Figs. 5.1-5.4 below with (a), (b) and (c) displaying the results for  $\mu = E_F$ ,  $\mu = W_1$ , and  $\mu = W_2$ , respectively. When the photon energy is smaller than 100 meV, there are peaks for all materials with a 10 meV smearing factor which doesn't show with the other two smearing



factors. However, these peaks can't be explained by the joint density of state (JDOS) since it's suppressed in the lower frequency region. Instead, the reason behind these peaks might be the transition of the Weyl band, which had also been found in several Weyl semimetals such as TaAs [54] and PrGeAl [32]. Among them, RhGe has the largest peak at  $E_F$  which is  $-488 \mu A/V^2$  at 0.012 eV. It's about half of TaAs  $\sigma_{xx}^z$  value. When  $\mu$  is shifted to  $W_1$  or  $W_2$ , the peak seems to reduce except for  $\mu$  being shifted to  $W_2$  of CoGe. Moreover, with the larger smearing factor of 38 meV or 100 meV, the low energy peaks disappear. However, the higher energy region looks similar for every smearing factor. Maybe it's because that a larger smearing factor can't show the feature of linear dispersion of the Weyl node properly. Recently, there's a study on the shift current of RhSi [53] and they also predicted the low energy peak.

CoSi

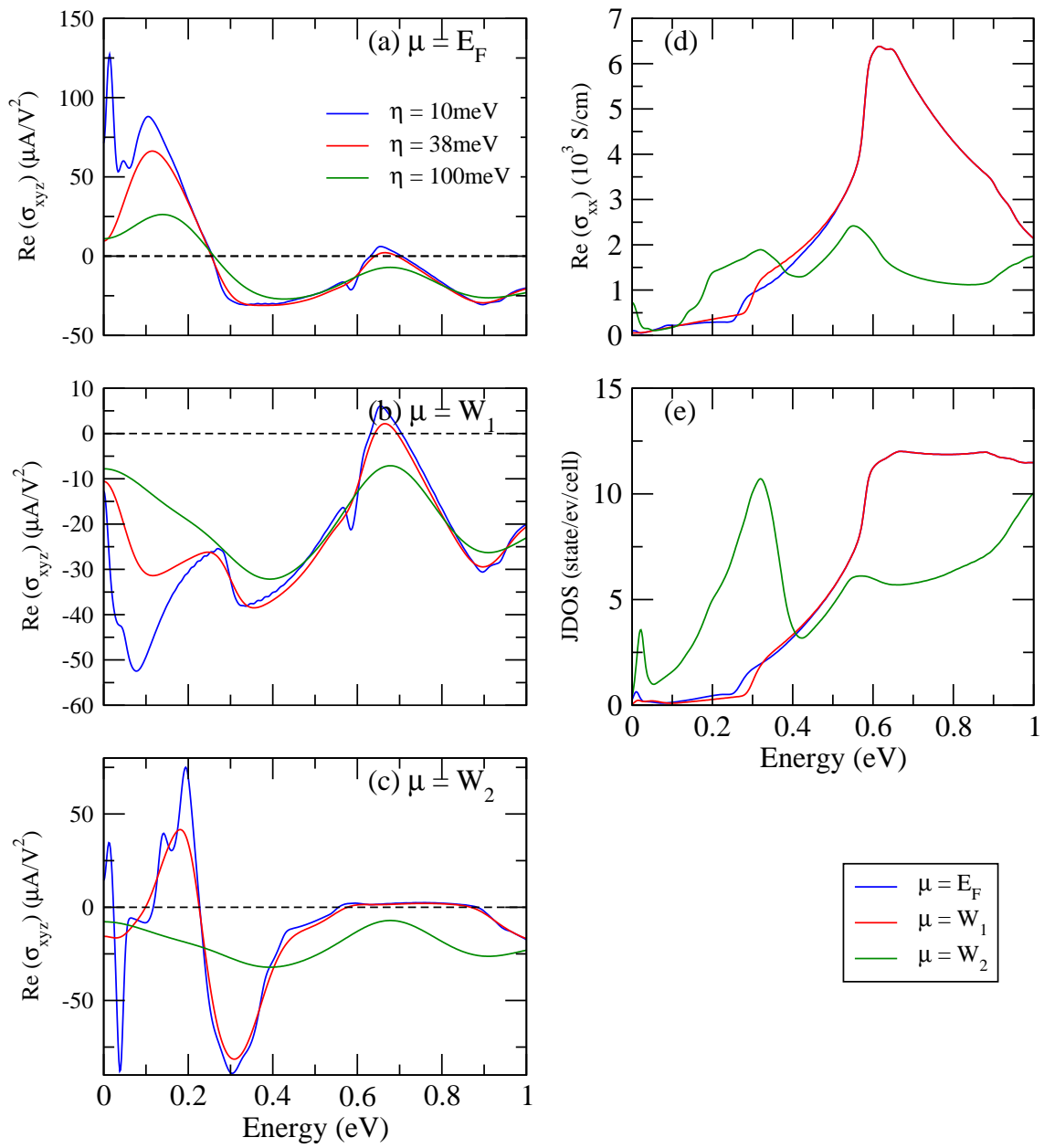
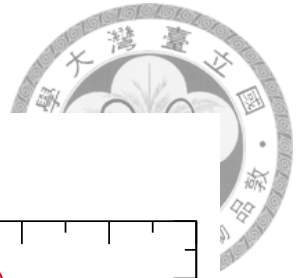


Figure 5.1: Left hand side of the plot is the calculated linear shift current of CoSi  $\sigma_{xyz}$  with (a)  $\mu = E_F$ , (b)  $\mu = W_1$ , and (c)  $\mu = W_2$ . On the right hand side is (d) real part of optical conductivity and (e) JDOS for CoSi.



CoGe

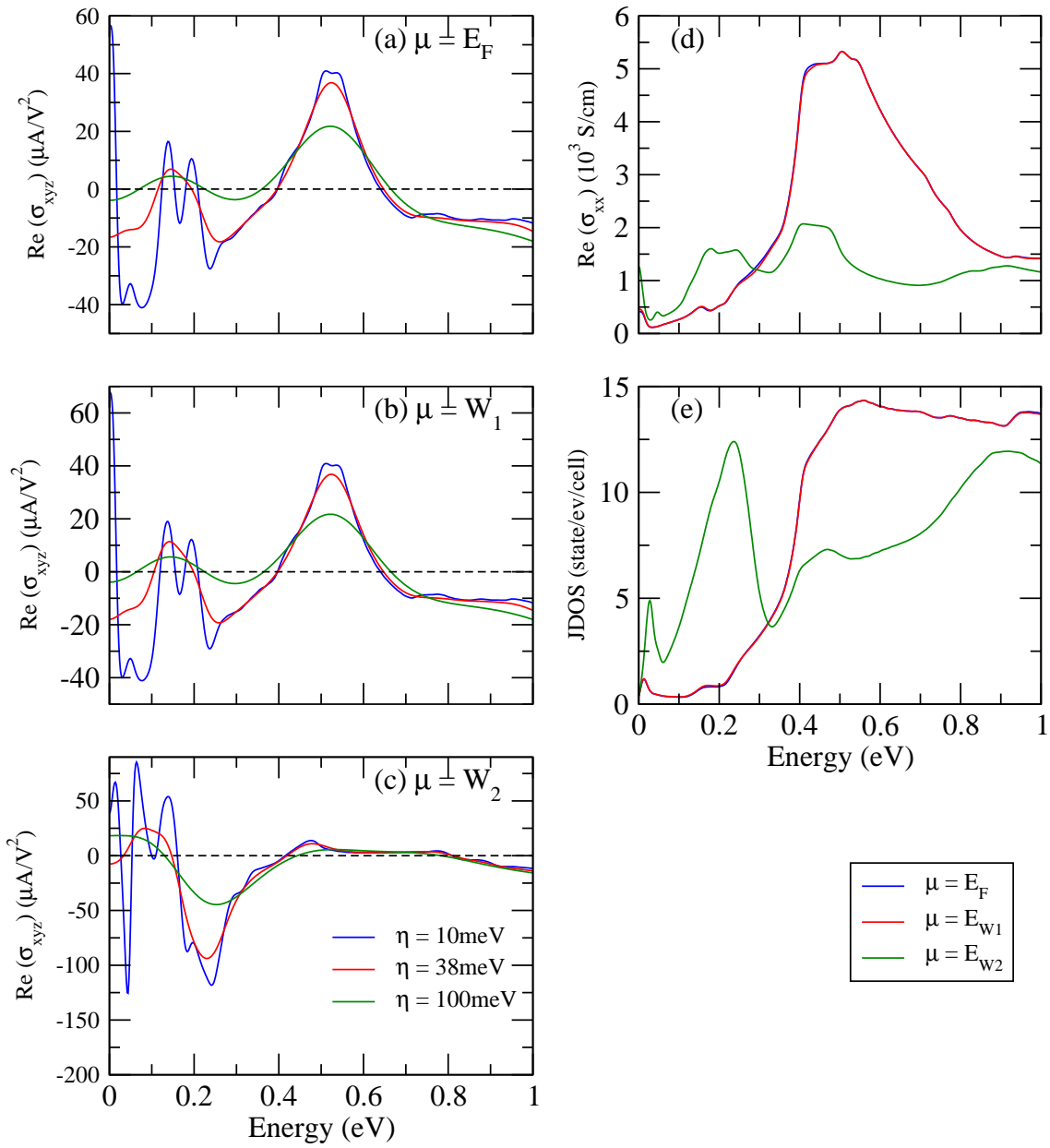
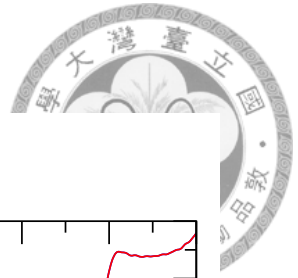


Figure 5.2: Left hand side of the plot is the calculated linear shift current of CoGe  $\sigma_{xyz}$  with (a)  $\mu = E_F$ , (b)  $\mu = W_1$ , and (c)  $\mu = W_2$ . On the right hand side is (d) real part of optical conductivity and (e) JDOS for CoGe.



RhSi

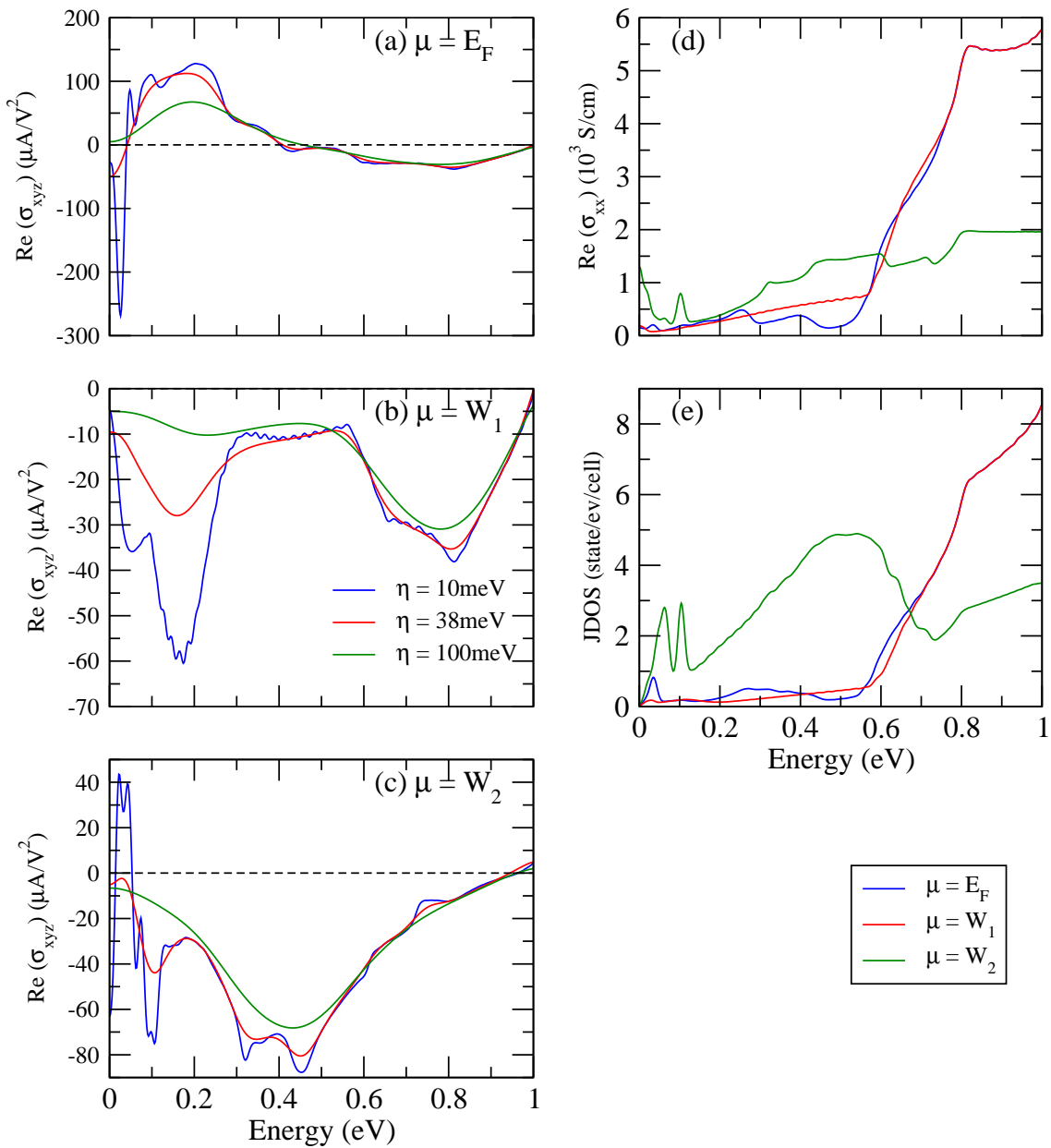
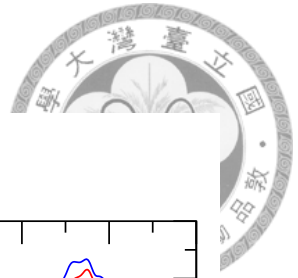


Figure 5.3: Left hand side of the plot is the calculated linear shift current of RhSi  $\sigma_{xyz}$  with (a)  $\mu = E_F$ , (b)  $\mu = W_1$ , and (c)  $\mu = W_2$ . On the right hand side is (d) real part of optical conductivity and (e) JDOS for RhSi.



RhGe

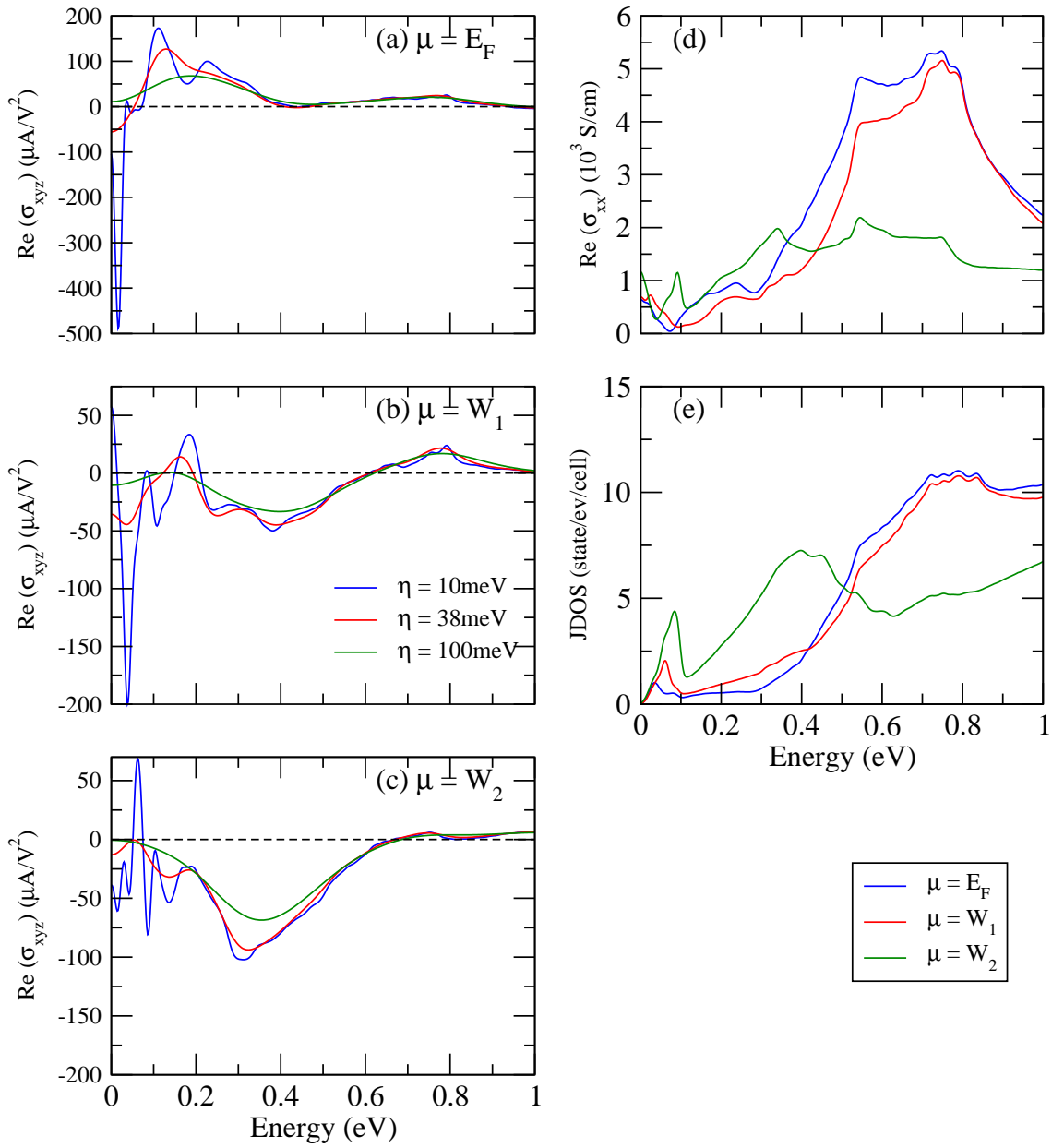
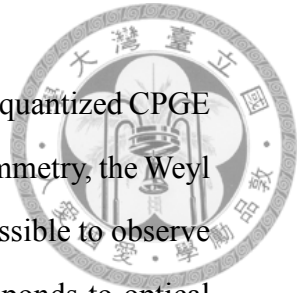


Figure 5.4: Left hand side of the plot is the calculated linear shift current of RhGe  $\sigma_{xyz}$  with (a)  $\mu = E_F$ , (b)  $\mu = W_1$ , and (c)  $\mu = W_2$ . On the right hand side is (d) real part of optical conductivity and (e) JDOS for RhGe.



For circular injection current, we will focus on the interesting feature, quantized CPGE [6], that might exist in chiral Weyl semimetals. Due to a lack of mirror symmetry, the Weyl nodes of chiral semimetal aren't located at the same energy level. It's possible to observe quantized CPGE when only one of the Weyl nodes is occupied and responds to optical transition. Tensor trace of CPGE  $\beta$  can be written as

$$\beta = iC\beta_0, \quad (5.1)$$

where  $\beta_0 = \frac{\pi e^3}{h^2}$  and  $C$  is the Chern number of the Weyl node. In CoSi family, there is no mirror symmetry in our system and the multifold Weyl nodes at  $\Gamma$  and  $R$  are separated to different energy. Also the large Chern numbers  $\pm 4$  make them a good platform to look for this effect.

CoSi family has only one independent tensor element  $\beta_{xx}$  ( $\beta_{xx}=\beta_{yy}=\beta_{zz}$ ) [44],  $\beta$  is simply  $3\beta_{xx}$ . For all materials we calculate the susceptibility of injection current and divide by  $\beta_0$  in Figs. 5.5-5.8 below with (a), (b), and (c) displaying the results of  $\mu = E_F$ ,  $\mu = W_1$ , and  $\mu = W_2$ , respectively. When we look at charge neutral point  $\mu = E_F$ , the injection current susceptibility has positive peak at around 0 eV to 0.2 eV region. However, all of them are smaller than  $\pm 4\beta_0$ , which is the quantized value that we are looking for. After we shift the chemical potential to  $\mu = W_1$ , CoSi shows a small plateau of  $4\beta_0$  around 0.2 eV with 10 meV smearing and RhSi show a broad plateau of  $4\beta_0$  between 0.3 eV to 0.6 eV with both 10 meV and 38 meV smearing, and this value is what we expect getting from Weyl node  $W_1$ . Nonetheless, CoGe and RhGe doesn't show any signal of quantized CPGE when  $\mu$  is shifted to  $W_1$ . The reason of absence of quantized CPGE for them might be that there are more trivial bands located at  $W_1$ . On the other hand, if we shift the chemical potential to  $W_2$ , all four materials show peaks or plateaus of  $-4\beta_0$  for 10 meV and 38 meV smearing. Among them, 0.3 eV to 0.6 eV of CoSi and 0.2 eV to 0.4 eV of CoGe seem to have the most steady quantized signal compared to RhSi and RhGe.

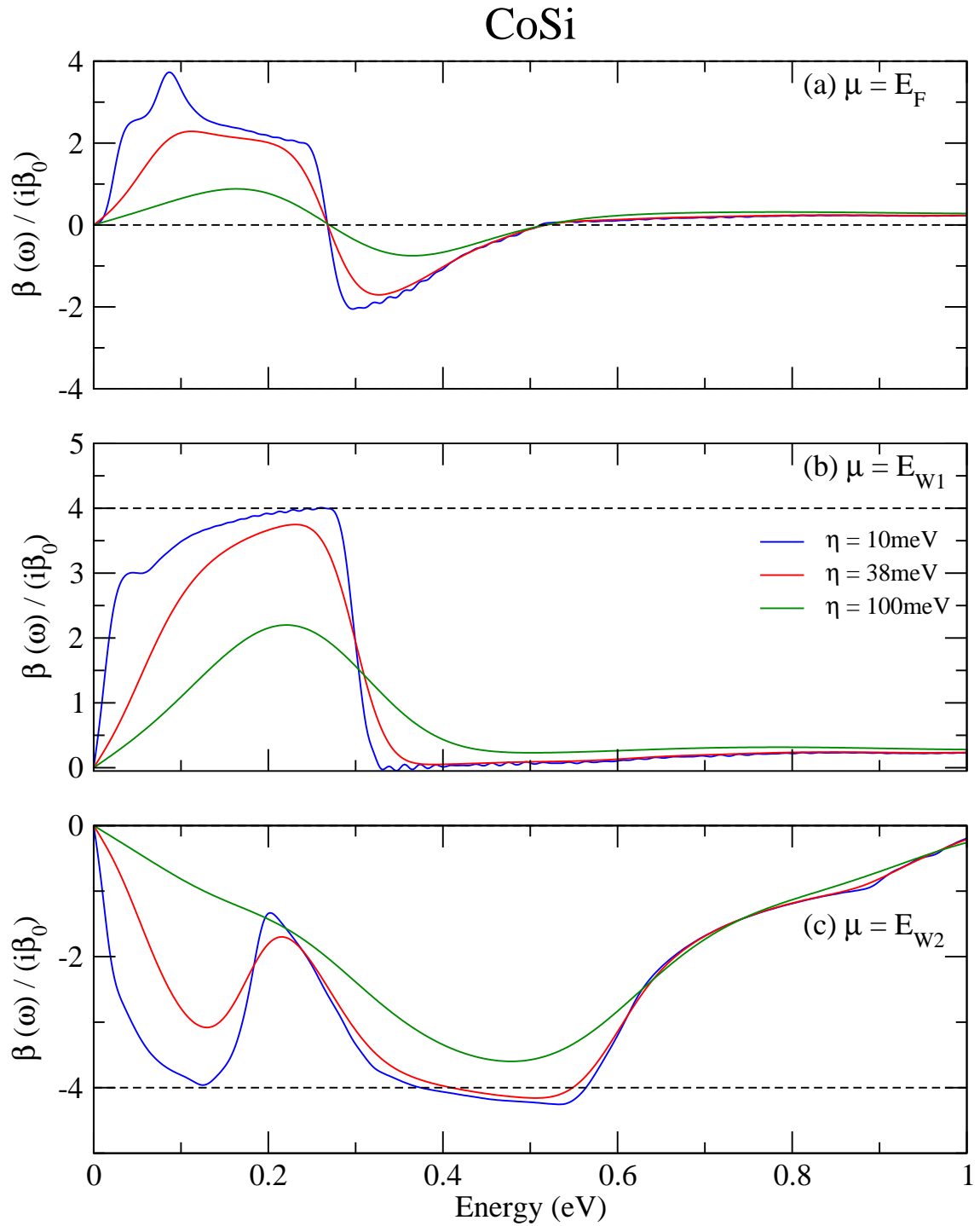


Figure 5.5: Circular injection current susceptibility  $\beta$  divide by  $\beta_0$  for CoSi when (a)  $\mu = E_F$ , (b)  $\mu = W_1$ , and (c)  $\mu = W_2$ .

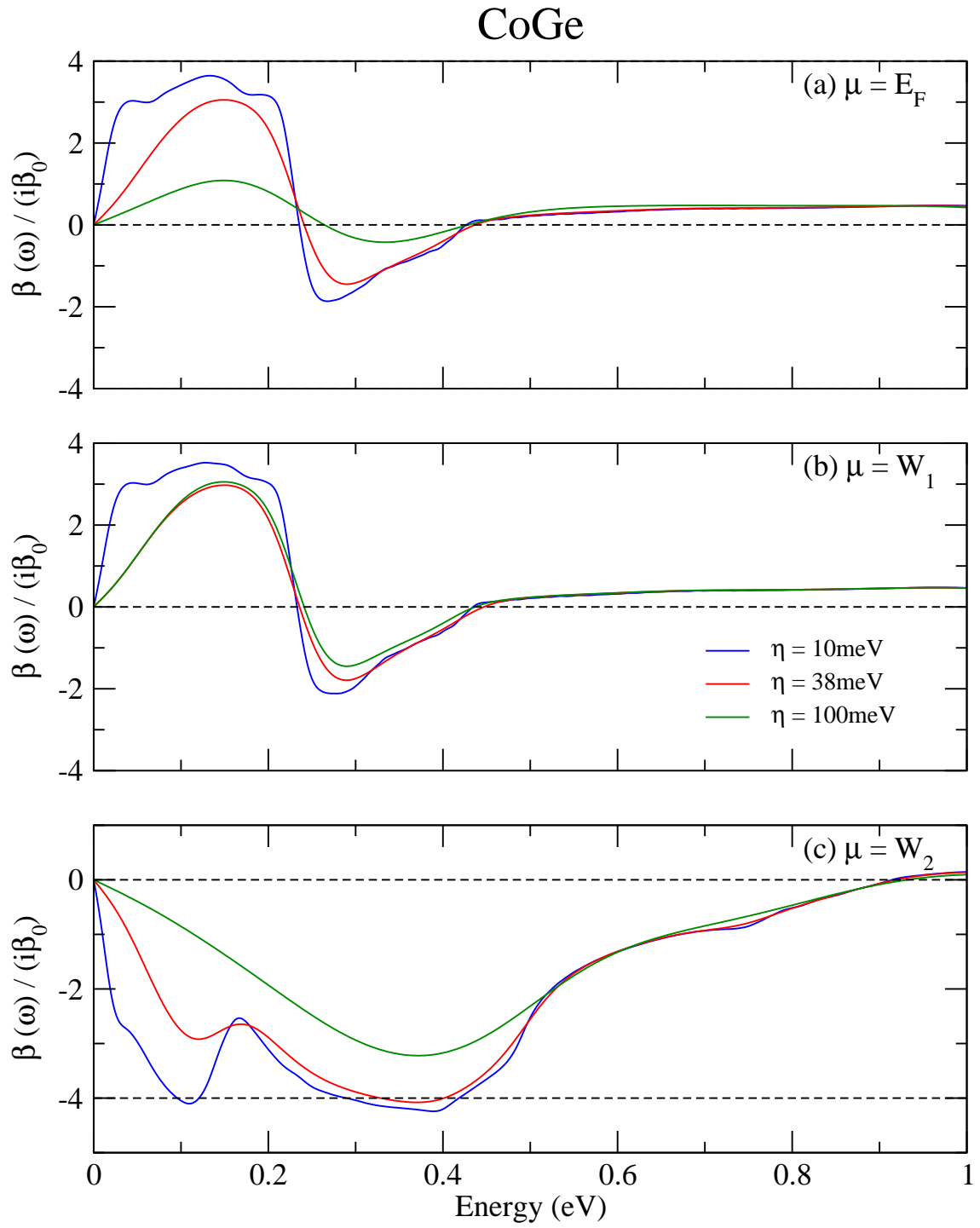


Figure 5.6: Circular injection current susceptibility  $\beta$  divide by  $\beta_0$  for CoGe when (a)  $\mu = E_F$ , (b)  $\mu = W_1$ , and (c)  $\mu = W_2$ .

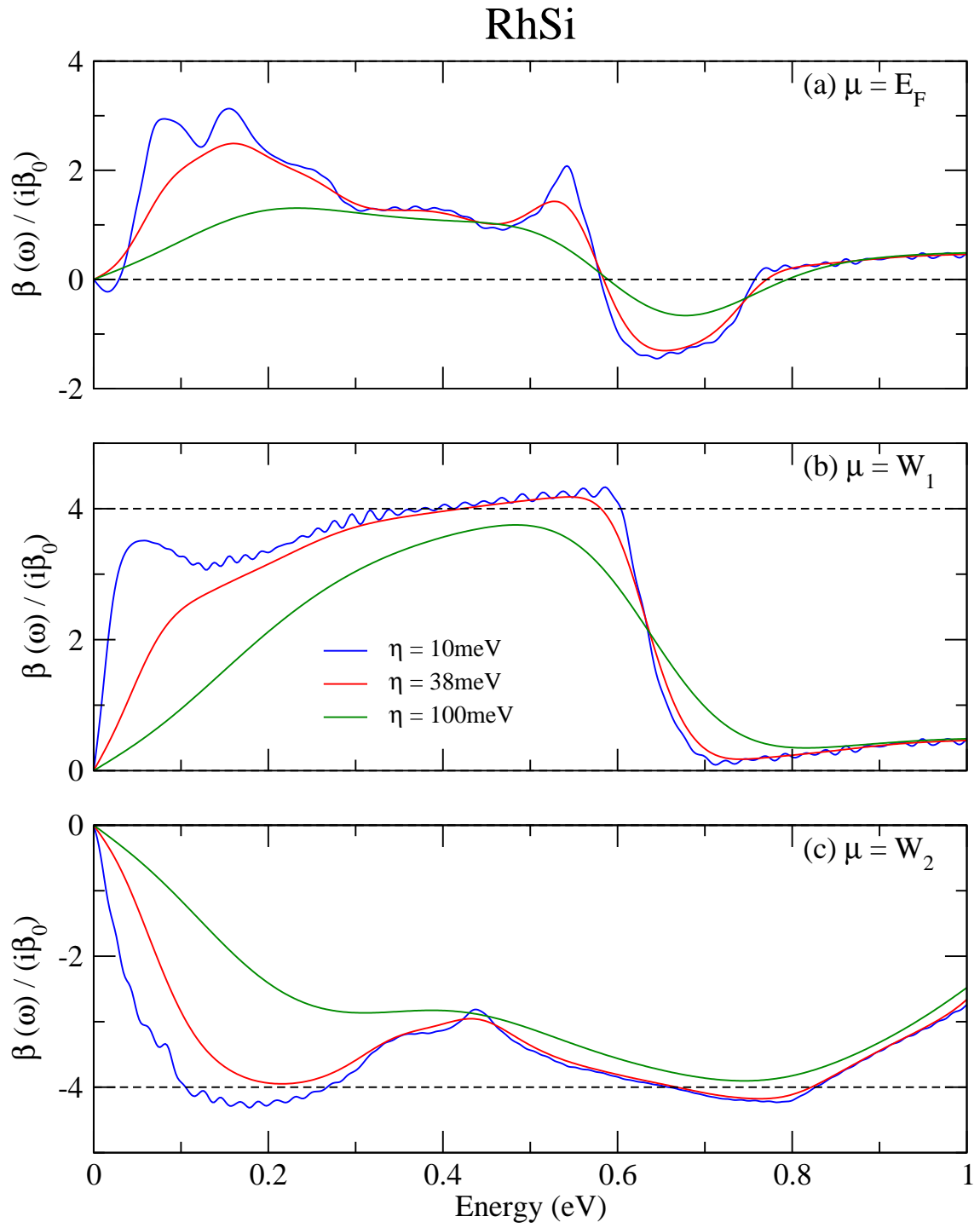


Figure 5.7: Circular injection current susceptibility  $\beta$  divide by  $\beta_0$  for RhSi when (a)  $\mu = E_F$ , (b)  $\mu = W_1$ , and (c)  $\mu = W_2$ .

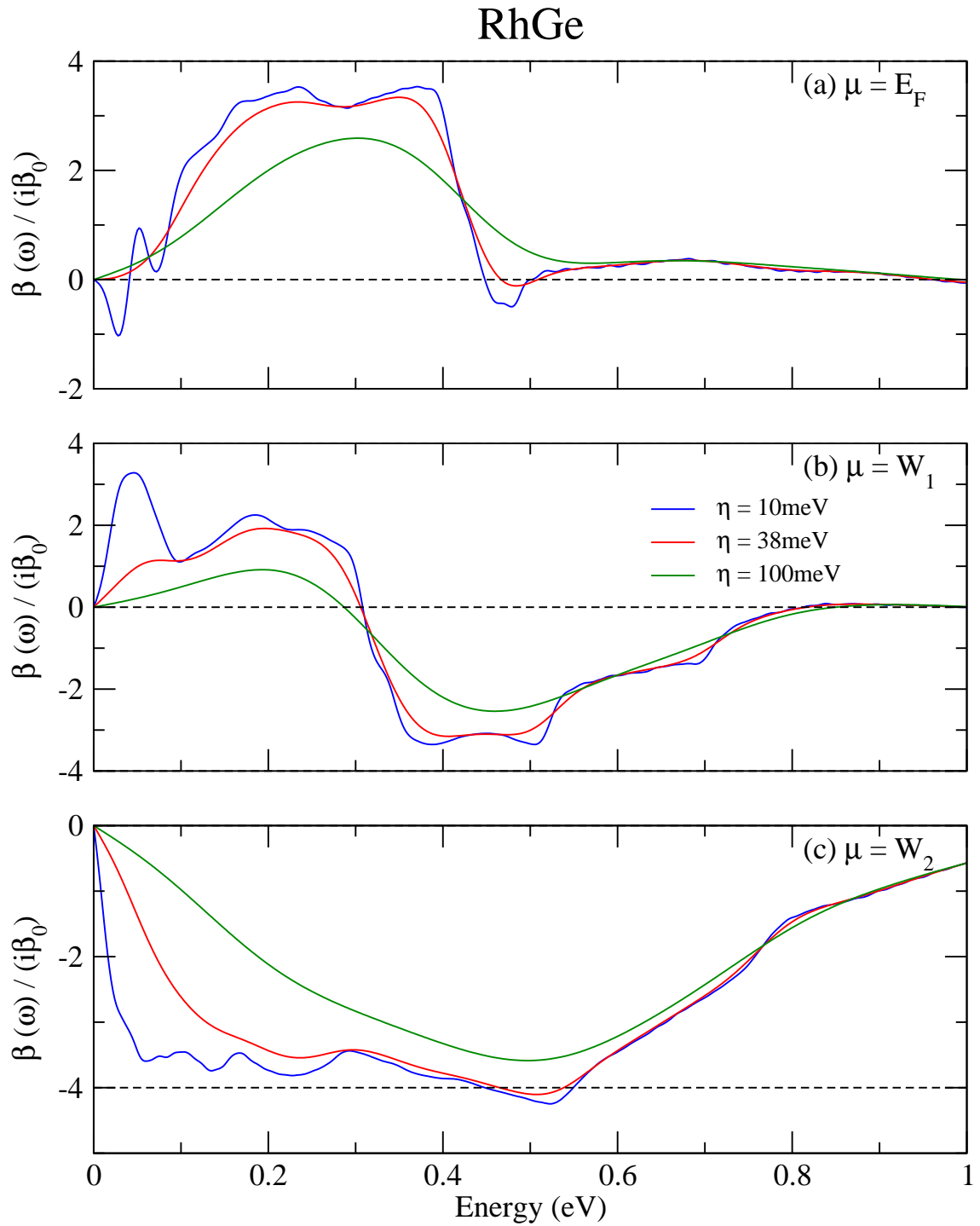


Figure 5.8: Circular injection current susceptibility  $\beta$  divide by  $\beta_0$  for RhGe when (a)  $\mu = E_F$ , (b)  $\mu = W_1$ , and (c)  $\mu = W_2$ .



## 5.2 Second harmonic generation

Same as shift current, there is also only one independent tensor element for SHG, i.e.,  $\chi_{xyz}^{(2)} = \chi_{yzx}^{(2)} = \chi_{zxy}^{(2)}$ . We plot the result of SHG with the 10 meV smearing factor in Figs. 5.9-5.12 below. The SHG for all four materials at  $\mu = E_F$ ,  $\mu = W_1$  and  $\mu = W_2$  at low frequency show divergence peaks as phonon frequency  $\omega$  approaches to zero. This divergent feature can't be explained from JDOS and might be the trait of Weyl semimetal. Recently the study of SHG of RhSi [56] also showed a similar shape. However, when they added the scissor correction, the divergences at low frequency disappear. A recent study on SHG of TaAs [55] also mentioned that the SHG  $\chi^{(2)}$  of Weyl semimetals would diverge as  $1/\omega$  as  $\omega$  goes to zero. Even the SHG of four materials have this divergence, they seem to behavior differently when we shift the chemical potential. For CoSi and RhGe, the value of SHG after shifting the chemical potential to  $\mu = W_2$  is much larger than  $\mu = W_1$  and  $\mu = E_F$ . As for CoGe and RhSi, however, the value of SHG after shifting to  $\mu = W_1$  is much larger than  $\mu = W_2$  and  $\mu = E_F$ . Moreover, the value of this larger SHG still maintains an extremely huge value even going to the higher energy region. Take CoSi for example, even with 1 eV photon energy, the SHG is still around  $2.7 \times 10^4$  (pm/V), which is large compared to the  $\chi_{zzz}^{(2)}$  of 7200 (pm/V) under 800 nm incident light reported for TaAs [55]. It would be interesting to calculate SHG for higher energy regions to further see the change. However, we only fitted the Wannier orbital around the Fermi level in this project, and thus we can only show the SHG result below 1 eV.

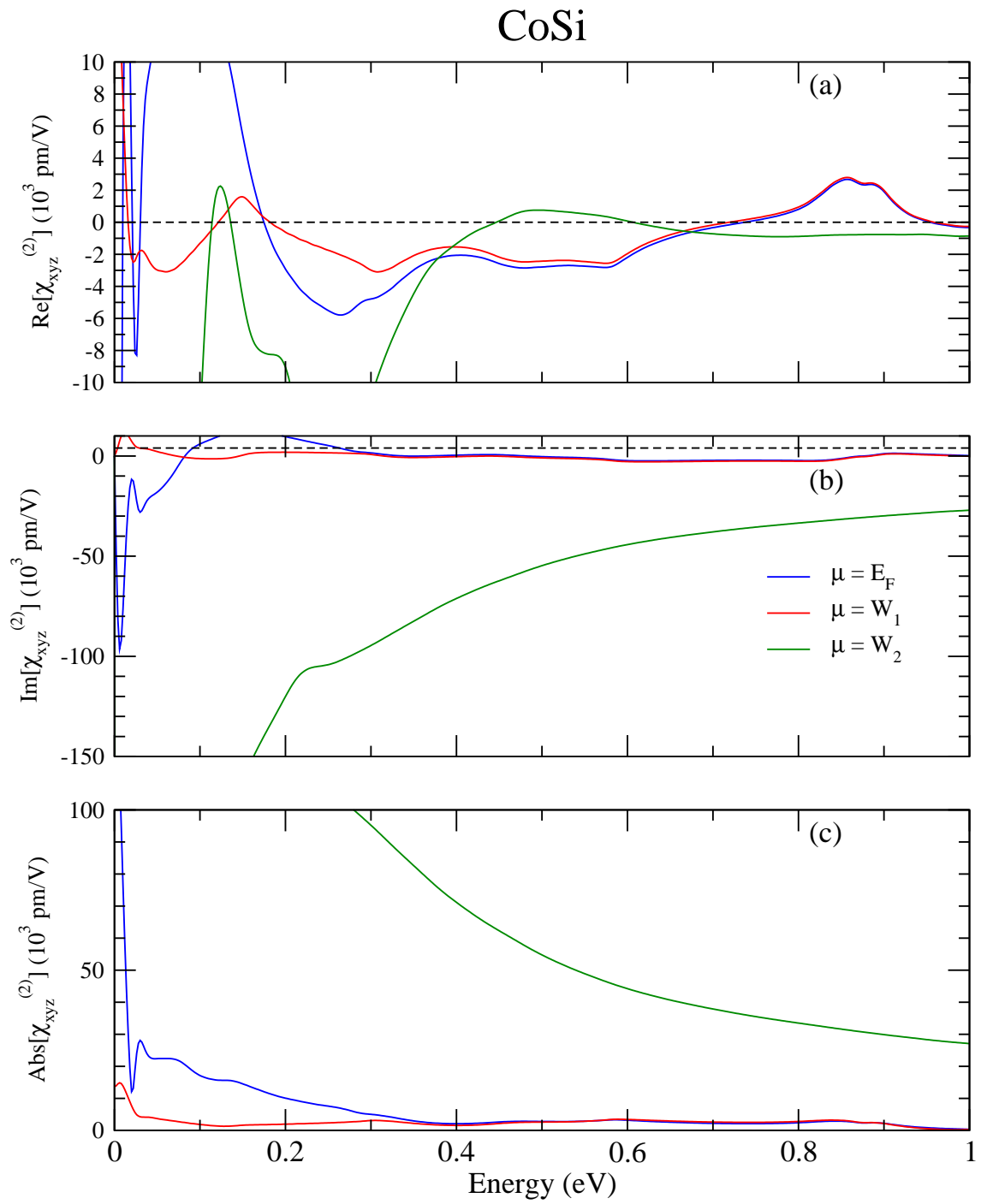


Figure 5.9: Real, imaginary, and absolute value of SHG of CoSi with (a)  $\mu = E_F$ , (b)  $\mu = W_1$ , and (c)  $\mu = W_2$ .

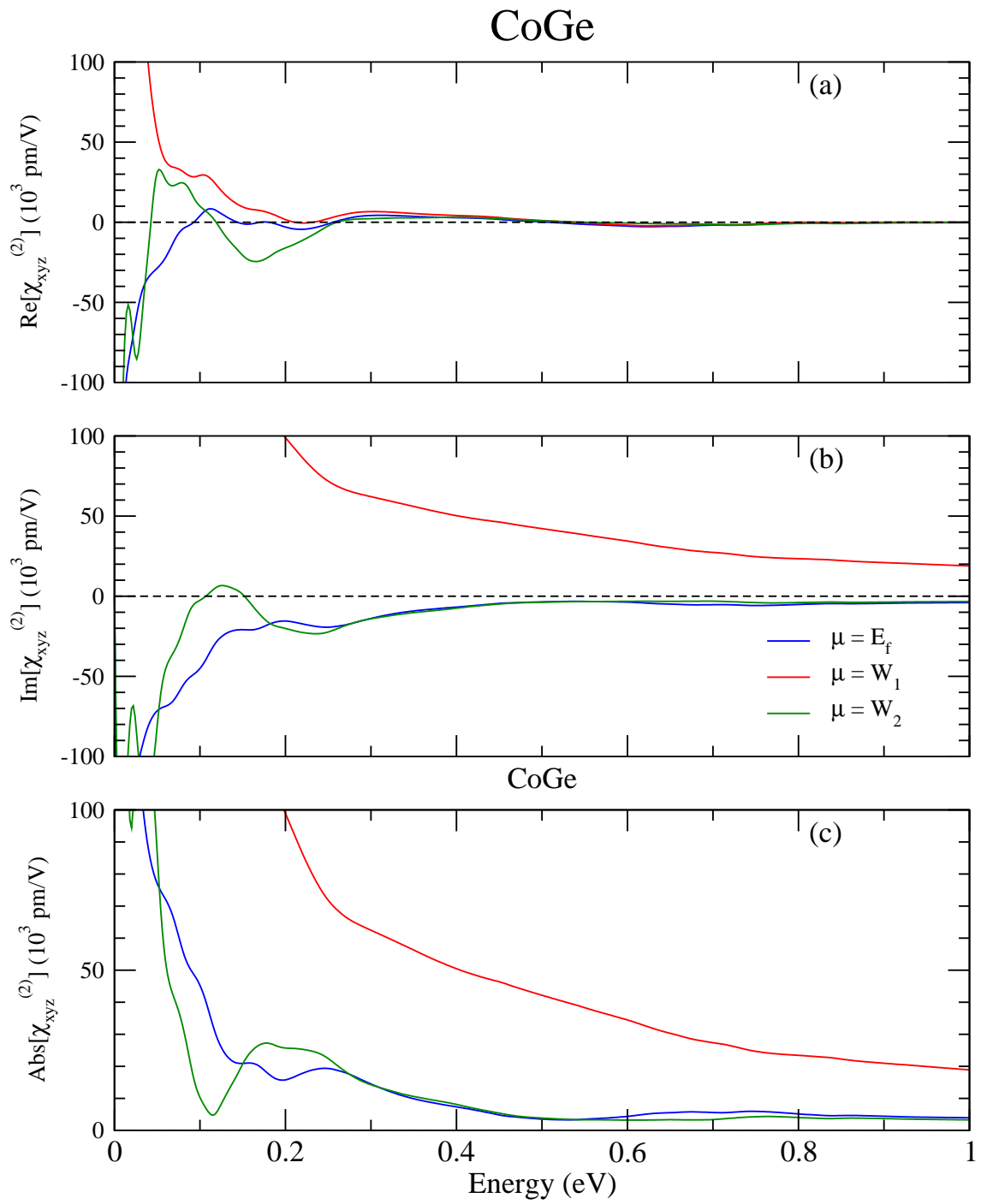


Figure 5.10: Real, imaginary, and absolute value of SHG of CoGe with (a)  $\mu = E_F$ , (b)  $\mu = W_1$ , and (c)  $\mu = W_2$ .

# RhSi

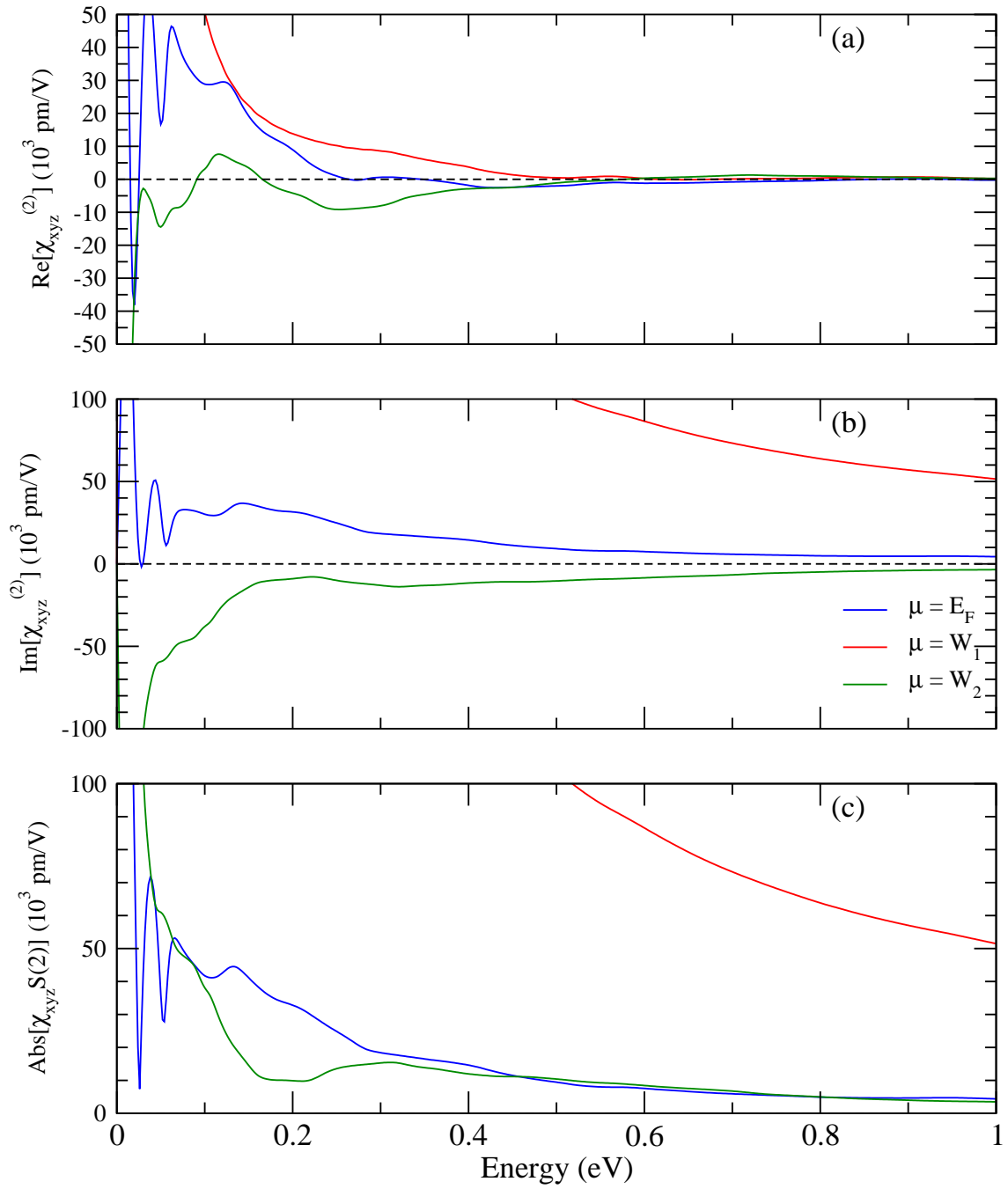


Figure 5.11: Real, imaginary, and absolute value of SHG of RhSi with (a)  $\mu = E_F$ , (b)  $\mu = W_1$ , and (c)  $\mu = W_2$ .

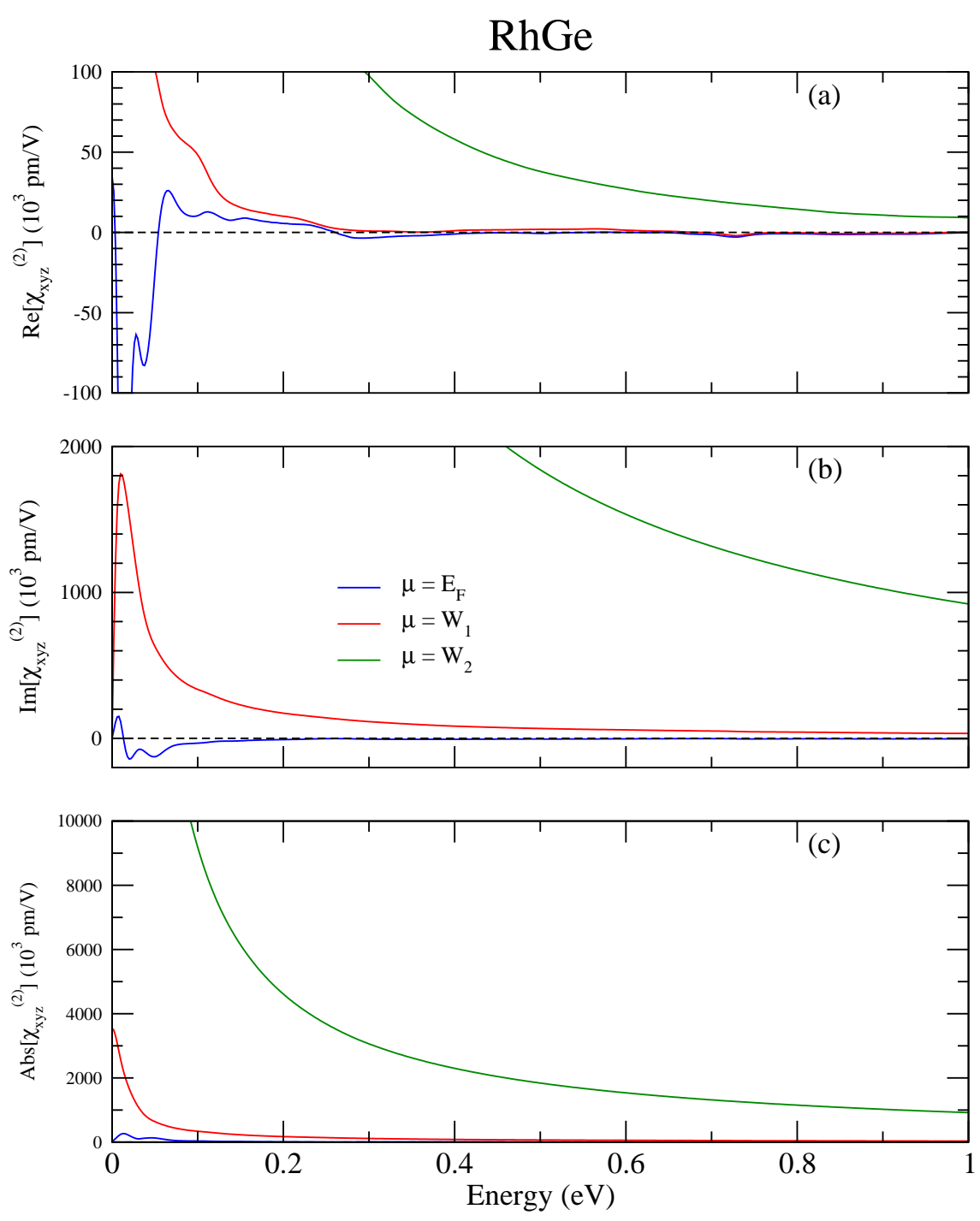


Figure 5.12: Real, imaginary, and absolute value of SHG of RhGe with (a)  $\mu = E_F$ , (b)  $\mu = W_1$ , and (c)  $\mu = W_2$ .



## Chapter 6

### Conclusion

In this thesis we systematically study spin transports and nonlinear optics of CoSi family. From the band structure we verify the multifold Weyl nodes with Chern number  $\pm 4$ . There are two kind of chirality for the structures, LHC and RHC. In CoSi family, only CoSi were experimentally synthesised for both LHC and RHC. Since the CoSi family break chiral symmetry, there are two independent tensor elements  $\sigma_{xy}^z$  and  $\sigma_{xz}^y$  for SHC. We calculate both tensor elements for CoSi family and find out the relation of SHC between LHC and RHC, suggesting that measuring SHC can be a way to check the chirality of the material. From SHC and SNC calculations, we find that RhGe has the largest SHC value with  $-139$  ( $\hbar/e$ )(S/cm) and CoGe has the largest SNC value with  $-1.25$  ( $\hbar/e$ )(A/m K). Even though the SHC is quite small compared to Pt, the spin Hall angle of RhSi and RhGe is around 7% and can be comparable to Pt due to their semimetallic nature. Moreover, by changing  $\mu$  to either  $W_1$  or  $W_2$  with hole doping or electron doping, the SHC and SNC can have a dramatically change.

For BPVE, we show that linear shift current has a peak at low frequency region, which is the trait of Weyl semimetals. Also, due to lack of mirror symmetry for CoSi family, it is possible to observe quantized circular injection current. We show that by shifting  $\mu$  to  $W_1$  for CoSi and RhSi there's clear plateau, and shifting to  $W_2$  for all materials we can get quantized CPGE signal. Also we show that the CPGE is quite sensitive to the change of hot-carrier lifetime  $\tau$  of the material. If the material has a longer hot-carrier lifetime it is more possible to observe these effect. Finally, we show that in low energy region the

SHG will diverge as  $1/\omega$  when  $\omega \rightarrow 0$ .





## Bibliography

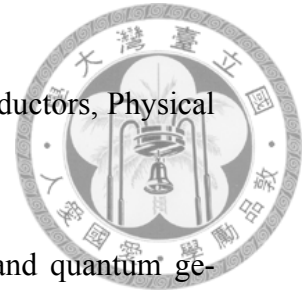
- [1] N. P. Armitage, E. J. Mele and A. Vishwanath, Weyl and Dirac semimetals in three-dimensional solids, *Rev. Mod. Phys.* **90**, 015001 (2018).
- [2] Y. Sun, Y. Zhang, C. Felser, and B. Yan, Strong Intrinsic Spin Hall Effect in the TaAs Family of Weyl Semimetals, *Phys. Rev. Lett.* **117**, 146403 (2016).
- [3] T. Ng, Y. Luo, J. Yuan, Y. Wu, H. Yang, and L. Shen, Origin and enhancement of the spin Hall angle in the Weyl semimetals LaAlSi and LaAlGe, *Phys. Rev. B* **104**, 014412 (2021).
- [4] Y. Yen and G.-Y. Guo, Tunable large spin Hall and spin Nernst effects in the Dirac semimetals ZrXY (X = Si, Ge; Y = S, Se, Te), *Phys. Rev. B* **101**, 064430 (2020).
- [5] B. B. Prasad and G.-Y. Guo, Tunable spin Hall and spin Nernst effects in Dirac line-node semimetals XCuYAs (X = Zr, Hf; Y = Si, Ge), *Phys. Rev. Materials* **4**, 124205 (2020).
- [6] F. de Juan, A. G. Grushin, T. Morimoto, and J. E. Moore, Quantized circular photogalvanic effect in Weyl semimetals, *Nat. Commun.* **8**, 15995 (2017).
- [7] Q. Xu, Y. Zhang, K. Koepf, W. Shi, J. van den Brink, C. Felser and Y. Sun, Comprehensive scan for nonmagnetic Weyl semimetals with nonlinear optical response, *npj Comput. Mater* **6**, 32 (2020).
- [8] C. Le, Y. Zhang, C. Felser, and Y. Sun, Ab initio study of quantized circular photogalvanic effect in chiral multifold semimetals, *Phys. Rev. B* **102**, 121111(R)(2020)



- [9] D. Rees, K. Manna, B. Lu, T. Morimoto, H. Borrmann, C. Felser, J. E. Moore, D. H. Torchinsky and J. Orenstein, Helicity-dependent photocurrents in the chiral Weyl semimetal RhSi, *Sci. Adv.* **6**, eaba0509 (2020)
- [10] H. Li, S. Xu, Z.-C. Rao, L.-Q. Zhou, Z.-J. Wang, S.-M. Zhou, S.-J. Tian, S.-Y. Gao, J.-J. Li, Y.-B. Huang, H.-C. Lei, H.-M. Weng, Y.-J. Sun, T.-L. Xia, T. Qian, and H. Ding, Chiral fermion reversal in chiral crystals, *Nat. Commun.* **10**, 5505 (2019).
- [11] B. Zhao, D. Khokhriakov, Y. Zhang, H. Fu, B. Karpiak, A. Md. Hoque, X. Xu, Y. Jiang, B. Yan, and S. P. Dash, Observation of charge to spin conversion in Weyl semimetal WTe<sub>2</sub> at room temperature, *Phys. Rev. Research* **2**, 013286 (2020).
- [12] P. Tang, Q. Zhou, and S.-C. Zhang, Multiple Types of Topological Fermions in Transition Metal Silicides, *Phys. Rev. Lett.* **119**, 206402 (2017).
- [13] Z. Rao, H. Li, T. Zhang, S. Tian, C. Li, B. Fu, C. Tang, L. Wang, Z. Li, W. Fan, J. Li, Y. Huang, Z. Liu, Y. Long, C. Fang, H. Weng, Y. Shi, H. Lei, Y. Sun, T. Qian, and H. Ding, Observation of unconventional chiral fermions with long Fermi arcs in CoSi, *Nature* **567**, 496 (2019).
- [14] Z. Ni, K. Wang, Y. Zhang, O. Pozo, B. Xu, X. Han, K. Manna, J. Paglione, C. Felser, A. G. Grushin et al., Giant topological longitudinal circular photo-galvanic effect in the chiral multifold semimetal CoSi, *Nat. Commun.* **12**, 154 (2021).
- [15] Z. Ni, B. Xu, M.-Á. Sánchez-Martínez, Y. Zhang, K. Manna, C. Bernhard, J. W. F. Venderbos, F. de Juan, C. Felser, A. G. Grushin et al, Linear and nonlinear optical responses in the chiral multifold semimetal RhSi, *npj Quantum Mater.* **5**, 96 (2020).
- [16] M. I. D'yakonov and V. I. Perel, Spin orientation of electrons associated with the interband absorption of light in semiconductors, *Sov. Phys. JETP* **33**, 1053 (1971).
- [17] S. Cheng, Y. Xing, Q.-F. Sun, and X. C. Xie, Spin Nernst effect and Nernst effect in two-dimensional electron systems, *Phys. Rev. B* **78**, 045302 (2008).
- [18] R. W. Boyd, *Nonlinear Optics*, 3rd ed.(2008)



- [19] P. Hohenberg and W. Kohn, Inhomogeneous electron gas, *Physical Review* **136**, B864 (1964).
- [20] W. Kohn, and L. J. Sham, Self-Consistent Equations Including Exchange and Correlation Effects, *Phys. Rev.* **140**, A1133 (1965).
- [21] J. P. Perdew and A. Zunger, Selfinteraction correction to densityfunctional approximations for manyelectron systems, *Physical Review B* **23**, 5048 (1981).
- [22] J. P. Perdew, K. Burke, and M. Ernzerhof, Generalized Gradient Approximation Made Simple, *Phys. Rev. Lett.* **77**, 3865 (1996)
- [23] C. S. Wang, B. M. Klein, and H. Krakauer, Theory of Magnetic and Structural Ordering in Iron, *Phys. Rev. Lett.* **16**, 1852 (1985)
- [24] G.Y.Guo, H. Ebert, W.M.Temmerman, K.Schwarz and P.Blaha, Relativistic effects on the structural and magnetic properties of iron, *Solid State Comm.* **79**, 121 (1991)
- [25] G. Y. Guo, and H. H. Wang, Gradient-corrected density functional calculation of structural and magnetic properties of BCC, FCC and HCP Cr, *J. Magn. Magn. Mater.* **209** (2000) 98–99
- [26] C. Kittel, *Introduction to Solid State Physics*. 8, (2004).
- [27] G. Y. Guo, S. Murakami, T.-W. Chen, and N. Nagaosa, Intrinsic Spin Hall Effect in Platinum: First-Principles Calculations, *Phys. Rev. Lett.* **100**, 096401 (2008).
- [28] D. Xiao, M.-C. Chang, and Q. Niu, Berry phase effects on electronic properties, *Rev. Mod. Phys.* **82**, 1959 (2010).
- [29] D. Xiao, Y. Yao, Z. Fang, and Q. Niu, Berry-Phase Effect in Anomalous Thermoelectric Transport, *Phys. Rev. Lett.* **97**, 026603 (2006).
- [30] C. Aversa and J. Sipe, Nonlinear optical susceptibilities of semiconductors: Results with a length-gauge analysis, *Physical Review B* **52**, 14636 (1995).



- [31] J. Sipe and A. Shkrebtii, Secondorder optical response in semiconductors, *Physical Review B* **61**, 5337 (2000).
- [32] J. Ahn, G.Y. Guo, and N. Nagaosa, Lowfrequency divergence and quantum geometry of the bulk photovoltaic effect in topological semimetals, *Physical Review X* **10**, 041041 (2020).
- [33] I. V. Kavich and L. P. Shevchuk, X-ray diffraction and X-ray spectrum examinations of the Co-Si-Ge system alloys, *Ukrainskii Fizicheskii Zhurnal (Russian Edition)* **23**, 624 (1978).
- [34] P. Demchenko, J. Kończyk, O. Bodak, R. Matvijishyn, L. Muratova, and B. Marciniak, Single crystal investigation of the new phase  $\text{Er}_{0.85}\text{Co}_{4.31}\text{Si}$  and of  $\text{CoSi}$ , *Chem. Met. Alloys* **1**, 50 (2008).
- [35] H. Takizawa, T. Sato, T. Endo, and M. Shimada, High-Pressure Synthesis and Electrical and Magnetic Properties of  $\text{MnGe}$  and  $\text{CoGe}$  with the Cubic B20 Structure, *J. Solid State Chem.* **73**, 40 (1988).
- [36] I. Engström and T. Johnsson, Least-squares Refinement of the Structure of  $\text{RhSi}$  ( $\text{FeSi}$ -type), *Acta Chem. Scand.* **19**, 1508 (1965).
- [37] V. I. Larchev and S. V. Popova, The polymorphism of transition metal monogermanides at high pressures and temperatures, *J. Less-Common Met.* **87**, 53 (1982).
- [38] G. Kresse and J. Hafner, *Ab initio* molecular dynamics for liquid metals, *Phys. Rev. B* **47**, 558 (1993).
- [39] G. Kresse and J. Furthmüller, Efficient iterative schemes for *ab initio* total-energy calculations using a plane-wave basis set, *Phys. Rev. B* **54**, 11169 (1996).
- [40] J. H. Ryoo, C.-H. Park, and I. Souza, Computation of intrinsic spin Hall conductivities from first principles using maximally localized Wannier functions, *Phys. Rev. B* **99**, 235113 (2019).



- [41] N. Marzari, A. A. Mostofi, J. R. Yates, I. Souza, and D. Vanderbilt, Maximally localized Wannier functions: Theory and applications, *Rev. Mod. Phys.* **84**, 1419 (2012).
- [42] G. Pizzi *et al.*, Wannier90 as a community code: new features and applications, *J. Phys.: Condens. Matter* **32**, 165902 (2020).
- [43] Q. S. Wu, S. N. Zhang, H.-F. Song, M. Troyer and A. A. Soluyanov, WannierTools: An open-source software package for novel topological materials, *Comput. Phys. Commun.* **224**, 405 (2018).
- [44] S. V. Gallego, J. Etxebarria, L. Elcoro, E. S. Tasci, and J. M. Perez-Mato, Automatic calculation of symmetry-adapted tensors in magnetic and non-magnetic materials: a new tool of the Bilbao Crystallographic Server, *Acta Cryst. A* **75**, 438 (2019).
- [45] E. Skoug, C. Zhou, Y. Pei and D. T. Morelli, High thermoelectric power factor in alloys based on CoSi, *Appl. Phys. Lett.* **94**, 022115 (2009).
- [46] N. Kanazawa, Y. Onose, Y. Shiomi, S. Ishiwata and Y. Tokura, Band-filling dependence of thermoelectric properties in B20-type CoGe, *Appl. Phys. Lett.* **100**, 093902 (2012).
- [47] L. Z. Maulana, K. Manna, E. Uykur, C. Felser, M. Dressel and A. V. Pronin, *Phys. Rev. Research* **2**, 023018 (2020).
- [48] V. A. Sidorov, A. E. Petrova, N. M. Chitchev, M. V. Magnitskaya, L. N. Fomicheva, D. A. Salamatin, A. V. Nikolaev, I. P. Zibrov, F. Wilhelm, A. Rogalev and A. V. Tsvyashchenko, Magnetic, electronic and transport properties of the high-pressure synthesized chiral magnets  $Mn_{1-x}Rh_xGe$ , *Phys. Rev. B* **98**, 125121 (2018).
- [49] H. L. Wang, C. H. Du, Y. Pu, R. Adur, P. C. Hammel and F. Y. Yang, Scaling of spin Hall angle in 3d, 4d, 5d metals from  $Y_3Fe_5O_{12}$ /metal spin pumping, *Phys. Rev. Lett.* **112**, 197201 (2014).
- [50] Y. K. Kato, R. C. Gossard and D. D. Awschalom, Observation of the spin Hall effect in semiconductors, *Science* **306**, 1910 (2004).



- [51] K. Tang, Y.-C. Lau, K. Nawa, Z. Wen, Q. Xiang, H. Sukegawa, T. Seki, Y. Miura, K. Takanashi, and S. Mitani, Spin Hall effect in a spin-1 chiral semimetal, *Phys. Rev. Research* **3**, 033101 (2021).
- [52] S. Meyer, Y.-T. Chen, S. Wimmer, M. Althammer, T. Wimmer, R. Schlitz, S. Geprägs, H. Huebl, D. Ködderitzsch, H. Ebert, G. E. W. Bauer, R. Gross, and S. T. B. Goennenwein, Observation of the spin Nernst effect, *Nat. Mater.* **16**, 977 (2017).
- [53] Z. Li, T. Iitaka, H. Zeng, and H. Su, Optical response of the chiral topological semimetal RhSi, *Phys. Rev. B* **100**, 155201. (2019)
- [54] Y. Zhang, H. Ishizuka, J. van den Brink, C. Felser, B. Yan, and N. Nagaosa, Photogalvanic Effect in Weyl Semimetals from First Principles, *Phys. Rev. B* **97**, 241118(R) (2018).
- [55] L. Wu, S. Patankar, T. Morimoto, N. L. Nair, E. Thewalt, A. Little, J. G. Analytis, J. E. Moore, and J. Orenstein, Giant anisotropic nonlinear optical response in transition metal monpnictide Weyl semimetals, *Nat. Phys.* **13**, 350. (2017)
- [56] B. Lu, S. Sayyad, M. Á. Sánchez-Martínez, K. Manna, C. Felser, A. G. Grushin, and D. H. Torchinsky, Second-harmonic generation in the topological multifold semimetal RhSi, *Phys. Rev. Research* **4**, L022022 (2022)
- [57] D. MacNeill, G. M. Stiehl, M. H. D. Guimaraes, R. A. Buhrman, J. Park, and D. C. Ralph, Control of spin-orbit torques through crystal symmetry in WTe<sub>2</sub>/ferromagnet bilayers, *Nat. Phys.* **13**, 300 (2017).
- [58] S. Shi, S. Liang, Z. Zhu, K. Cai, S. D. Pollard, Y. Wang, J. Wang, Q. Wang, P. He, J. Yu, G. Eda, G. Liang, and H. Yang, All-electric magnetization switching and Dzyaloshinskii-Moriya interaction in WTe<sub>2</sub>/ferromagnet heterostructures, *Nat. Nanotechnol.* **14**, 945 (2019).